Mon. Not. R. Astron. Soc. **000**, 1–17 (2002) Printed 10 January 2014 (MN LATEX style file v2.2)

Multi-frequency study of a new Fe-rich supernova remnant in the Large Magellanic Cloud, MCSNR J0508–6902

L. M. Bozzetto,[1] P. J. Kavanagh,[2] P. Maggi,[3] M. D. Filipović,[1] M. Stupar,[4,5] Q. A. Parker,[4,5,6] W. A. Reid,[4,5] M. Sasaki,[2] F. Haberl,[3] D. Urošević,[7,8] J. Dickel,[9] R. Sturm,[3] R. Williams,[10] M. Ehle,[11] R. Gruendl,[12] Y.-H. Chu,[12] S. Points,[13] & E. J. Crawford[1]

[1] *University of Western Sydney, Locked Bag 1797, Penrith South DC, NSW 1797, Australia*
[2] *Institut für Astronomie und Astrophysik Tübingen, Universität Tübingen, Sand 1, 72076 Tübingen, Germany*
[3] *Max-Planck-Institut für extraterrestrische Physik, Giessenbachstraße, D-85748 Garching, Germany*
[4] *Department of Physics, Macquarie University, Sydney, NSW 2109, Australia*
[5] *Australian Astronomical Observatory, PO Box 296, Epping, NSW 1710, Australia*
[6] *Research Centre for Astronomy, Astrophysics and Astrophotonics, Macquarie University, Sydney, NSW 2109 Australia*
[7] *Department of Astronomy, Faculty of Mathematics, University of Belgrade, Studentski trg 16, 11000 Belgrade, Serbia*
[8] *Isaac Newton Institute of Chile, Yugoslavia Branch*
[9] *Physics and Astronomy Department, University of New Mexico, MSC 07-4220, Albuquerque, NM 87131, USA*
[10] *Coca-Cola Space Science Center, 701 Front Avenue, Columbus, GA 31901*
[11] *XMM-Newton Science Operations Centre, ESAC, ESA, PO Box 78, 28691 Villanueva de la Cañada, Madrid, Spain*
[12] *Department of Astronomy, University of Illinois, 1002 West Green Street, Urbana, IL 61801, USA*
[13] *Cerro Tololo Inter-American Observatory, Casilla 603, La Serena, Chile*

arXiv:1401.1868v1 [astro-ph.HE] 9 Jan 2014

Released 2011 Xxxxx XX

ABSTRACT

We present a detailed radio, X-ray and optical study of a newly discovered Large Magellanic Cloud (LMC) supernova remnant (SNR) which we denote MCSNR J0508–6902. Observations from the Australian Telescope Compact Array (ATCA) and the *XMM-Newton* X-ray observatory are complemented by deep Hα images and Anglo Australian Telescope AAOmega spectroscopic data to study the SNR shell and its shock-ionisation. Archival data at other wavelengths are also examined. The remnant follows a filled-in shell type morphology in the radio–continuum and has a size of $\sim$74 pc $\times$ 57 pc at the LMC distance. The X-ray emission exhibits a faint soft shell morphology with Fe-rich gas in its interior – indicative of a Type Ia origin. The remnant appears to be mostly dissipated at higher radio-continuum frequencies leaving only the south-eastern limb fully detectable while in the optical it is the western side of the SNR shell that is clearly detected. The best-fit temperature to the shell X-ray emission ($kT = 0.41^{+0.05}_{-0.06}$ keV) is consistent with other large LMC SNRs. We determined an O/Fe ratio of < 21 and an Fe mass of 0.5–1.8 $M_{\odot}$ in the interior of the remnant, both of which are consistent with the Type Ia scenario. We find an equipartition magnetic field for the remnant of $\sim$28 μG, a value typical of older SNRs and consistent with other analyses which also infer an older remnant.

Key words: ISM: supernova remnants, (galaxies:) Magellanic Clouds, radio continuum: ISM, X-rays: ISM

1 INTRODUCTION

The study of supernova remnants is an imperative part in our understanding of the universe, as they have a profound effect on their surrounding environment. SNRs distribute heavy elements throughout the galaxy, with thermonuclear (Type Ia) explosions contributing a significant amount of iron into the surrounding medium, whilst core-collapse supernovae (SNe) inject large amounts of Oxygen and other α elements (Matteucci & Greggio 1986). Type Ia SNe are thought to arise when a C-O white dwarf (in a binary system) approaches the Chandrasekhar limit. This occurs either through accretion from the binary companion, or by a merger with a white dwarf companion, and is currently actively debated (see e.g. Maoz 2008 and references therein).

Core-collapse SNe are believed to be the result of a progenitor star (with a main sequence mass above 8 solar masses) being drained of its nuclear fuel and therefore not being able to hold up against its own gravity through the release of nuclear energy.

The Large Magellanic Cloud (LMC) is an irregular dwarf galaxy located in close proximity (50 kpc, di Benedetto 2008) to our own Galaxy, allowing modern instruments to reach high sensitivity levels with sufficient angular resolution, from radio to X-ray wavelengths. At this distance, and because of its moderate inclination angle of 35° (van der Marel & Cioni 2001), we are able to assume objects which lay within it are all at a similar distance. This allows us to analyse the surface brightness and spatial extent of an object accurately, which is often difficult in our own Galaxy due to uncertainties in distance, foreground absorption, and background confusion. Furthermore, the LMC is considered an almost ideal environment for the study of a wide range of celestial objects due to the presence of active star-forming regions and its location outside of the Galactic plane, where absorption by gas and dust is reasonably low.

Several multi-wavelength SNR selection criteria exist in the literature (e.g. Fesen et al. 1985) as well as the powerful, newly evaluated emission-line diagnostic criteria reported by Frew & Parker (2010) and updated in Sabin et al. (2013). These are based on the well-known Sabbadin et al. (1977; hereafter SMB) SMB Hα/[N II] versus Hα/[S II] diagnostic diagram and the Baldwin et al. (1981; hereafter BPT) BPT [O III]5007/Hβ versus [S II]/Hα diagnostic diagrams. In this paper we adopt the criteria used by the Magellanic Cloud Supernova Remnant (MCSNR) Database[1] which are effectively compatible with these publications. In this classification system, a SNR must satisfy at least two of the following three observational criteria: significant Hα, [S II], and/or [O III] optical line emission with an observed [S II]/Hα flux ratio of > 0.4 (Mathewson & Clarke 1973); extended non-thermal radio emission indicative of synchrotron radiation (Filipovic et al. 1998) and extended thermal X-ray emission.

The ROSAT position sensitive proportional counter (PSPC) catalogue of X-ray sources in the LMC (Haberl & Pietsch 1999) contains the object [HP99] 791. While this source was confirmed as extended, its large off-axis angle prevented a reliable classification at that time. In this paper, we present new radio-continuum and X-ray observations of [HP99] 791, from the Australia Telescope Compact Array (ATCA) and *XMM-Newton*, respectively. We also present for the first time the clear identification of an unambiguous complete optical shell for the remnant from a deep arcsecond-resolution Hα image, a multi-exposure stack of the central 25 square degrees of the LMC (Reid & Parker 2006a). The shell can also be seen at lower resolution in the Magellanic Clouds Emission Line Survey (MCELS) data. Finally, we present new optical spectra from several components on the enhanced western side of the optical shell taken by the AAOmega spectrograph on the AAT (Saunders et al. 2004, Sharp et al. 2006) which confirm a strong signature of shock excitation as expected for an SNR. This new discovery clearly satisfies all three criteria for identification as a bona-fide SNR and so we assign to the source the identifier MCSNR J0508–6902 following the MCSNR Database nomenclature.

The observations used in this project are described in Section 2, followed by the data analysis in Section 3. The results from these observations are explained in Section 4 and then discussed in Section 5.

2 OBSERVATIONS

2.1 Radio

The ATCA is a radio interferometer located in northern New South Wales, Australia. Its new 2 GHz bandwidth and improved sensitivity has made it possible to obtain observations of a previously poorly studied group of SNRs, the older and more evolved SNRs that were not detected so far. We observed MCSNR J0508–6902 on the 15$^{\rm th}$ and 16$^{\rm th}$ of November 2011 with the ATCA, using the new compact array broadband backend (CABB) receiver in the array configuration EW367, at wavelengths of 3 and 6 cm (ν=9000 and 5500 MHz). Baselines formed with the 6$^{\rm th}$ ATCA antenna were omitted, as the other five antennas were arranged in a compact configuration. The observations were carried out in the so called 'snap-shot' mode, totalling ∼50 minutes of integration over a 14 hour period. The source PKS B1934-638 was used for primary (flux) calibration and the source PKS B0530-727 was used for secondary (phase) calibration. The phase calibrator was observed for a period of 2 minutes every half hour during the observations.

In addition to our own observations, we made use of a 36 cm (843 MHz) Molonglo Synthesis Telescope (MOST) mosaic image (as described in Mills et al. 1984), a 20 cm (1400 MHz) mosaic image (Hughes et al. 2007) as well as 6 cm (4800 MHz) and 3 cm (8640 MHz) mosaic images from project C918 (Dickel et al. 2005).

2.2 X-ray

Haberl & Pietsch (1999) detected this source in their compilation of ROSAT PSPC observations, recording an X-ray position of RA(J2000)=$05^h08^m36.7^s$, DEC(J2000)=–69°02′54″, and an extent of 43.6″. It is listed as [HP99] 791. However, due to the large off-axis angle of the source, a classification was not possible.

We observed MCSNR J0508–6902 with *XMM-Newton* on two occasions: in May 2010 (Obs. ID 0651880201, PI M. Sasaki), and, more recently, in September 2012 (Obs. ID 0690752001, PI F. Haberl) as part of the LMC survey. The European Photon imaging Camera (EPIC) onboard *XMM-Newton* (Jansen et al. 2001) consists of a pn CCD (Strüder et al. 2001) and two MOS CCD imaging spectrometers (Turner et al. 2001). The observational data were reduced using the standard reduction tasks of SAS[2] version 12.0.1, filtering for periods of high particle background. Unfortunately, Obs. ID 0651880201 was blighted by very high background, resulting in only ∼ 9 ks of the exposure being useful. However, in the case of Obs. ID 0690752001, there was virtually no background contamination with almost all data (∼ 25 ks) available for further analysis.

[1] See `http://www.mcsnr.org/about.aspx`

[2] Science Analysis Software, see `http://xmm.esac.esa.int/sas/`

2.3 Optical: Imaging and Spectroscopy

We have used deep, arcsecond-resolution, narrow-band optical Hα images created from a median stack of a dozen 2 hour exposures on the central 25 square degrees of the LMC as described in detail by Reid & Parker (2006a). These data have been used as the basis for unprecedented new discoveries of emission line sources in general and Planetary Nebulae (PN) in particular across the central LMC (e.g. Reid & Parker 2006a,b, 2012). The survey filter, detector and other parameters are described by Parker et al. (2005) but in essence the LMC multiple exposures were taken with fine-grained Kodak Tech-Pan films on the UK Schmidt Telescope using a monolithic interference filter of exceptional quality (e.g. Parker & Bland-Hawthorn 1998). These exposures were scanned with the SuperCOSMOS measuring machine (Hambly et al. 2001), (included with an in-built accurate WCS) transformed into electronic form and then median stacked to reach depths of $R_{equiv}\sim22$ for Hα (4.5×10^{-17} erg cm^{-2} s^{-1}Å^{-1}). We extracted Hα and matching SR (short 'broad-band' red) fits images over a $6'\times6'$ area centered on the SNR with 10 μm (0.67") pixels from the median-stacked images to create a quotient image (Hα divided by the SR) as shown in Fig. 1 reproduced to clip to the inner 98% of intensity values. North-east is to the top left. A complete oval shell can be seen in Hα but with the western side being enhanced. The centroid of this oval shell and hence the best estimate for the optical centre of the remnant is RA(J2000)=$05^h08^m33.7^s$ and DEC(J2000)=–69°02′33″. The major axis is 4.5′ in extent and the minor axis only 4′. The positions of the 2dF spectral samples obtained are also indicated on the figure (see below for further details).

We also checked for detection of the SNR in the Magellanic Cloud Emission Line Survey (MCELS) that was carried out with the 0.6 m University of Michigan/CTIO Curtis Schmidt telescope, equipped with a SITE 2048×2048 CCD, which gave a field of 1.35° at a scale of 2.3″ pixel^{-1} (∼5 arcsec resolution). Both the LMC and SMC were mapped in narrow bands corresponding to Hα, [O III] (λ=5007 Å), and [S II] (λ=6716, 6731 Å). All the data have been flux-calibrated and assembled into mosaic images, a small section of which is shown in Fig. 2. Further details regarding the MCELS are given by Smith et al. (2006) and at http://www.ctio.noao.edu/mcels. The MCELS data also reveal the SNR though at the poorer angular resolution it is hard to discern the full oval optical shell. However, MCELS does have the added advantage of the [O III] and [S II] filters providing additional diagnostic capabilities. The composite RGB image with (R=Hα, G=[SII], and B= [OIII]) centred on the new SNR is shown in Fig. 2 with the *XMM-Newton* contours in red (0.7–1.1 keV) and ATCA 5500 MHz radio data contours in white. Interestingly the strongest radio signature corresponds to the weakest optical emission to the south-east while the X-ray emission occupies the centre of the shell.

2.3.1 AAT AAOmega spectroscopy

As part of an AAOmega 2dF (two degree field) service night on the AAT on May 1st 2013, 2×900 second exposures were taken on an LMC 2-degree field centred at RA(J2000)=$05^h13^m15.7^s$ and DEC(J2000)=–69°29′51″ for

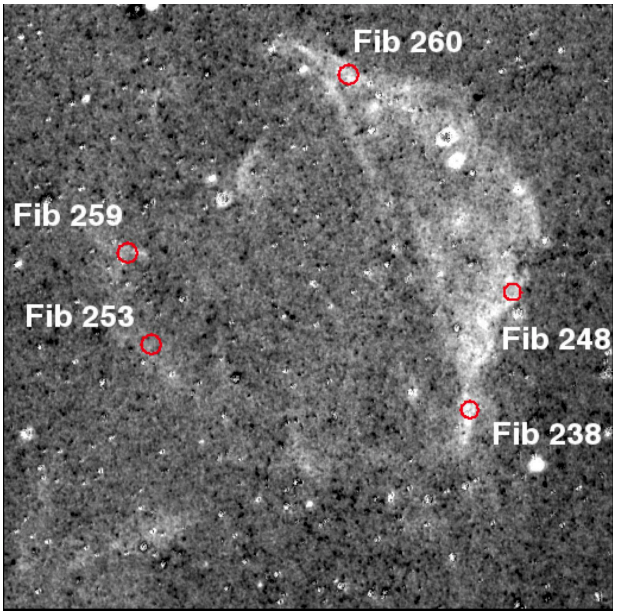

Figure 1. Hα quotient image of the new SNR MCSNR J0508–6902 taken from the data of Reid & Parker (2006a) revealing the complete optical oval shell for the first time but with enhanced emission on the western side. The positions of the 2dF fibres for the optical spectroscopy are indicated. The image is $\sim 6'\times6'$ on a side and north-east is to the top left.

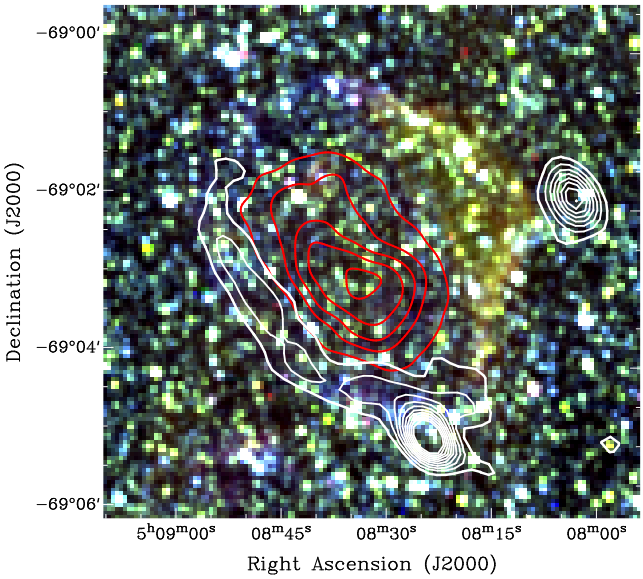

Figure 2. MCELS composite optical image (RGB =Hα,[SII],[OIII]) of MCSNR J0508–6902 overlaid with *XMM-Newton* contours (0.7–1.1 keV; red) of 7, 14, 21, 28 & 35×10^{-6} cts/s and ATCA (5500 MHz; white) contours from 3σ to 30σ in steps of 3σ.

Table 1. AAOmega fibre ID and fibre positions and line ratios for the spectral samples taken across the SNR as labelled in Fig.1. All line intensities are relative and extinction across the limited wavelength range of these emission lines is ignored. Errors in relative flux for observed lines are ∼10%.

2df fibre ID	RA (J2000)	DEC (J2000)	[S II]/Hα	Hα	[S II]6717	[S II]6731	[S II]6717/6731	Comments
Fib 238	05 08 16.2	–69 03 34	0.62	938	372	209	1.8	Low density limit
Fib 248	05 08 13.0	–69 02 41	0.76	1241	638	301	2.2	Low density limit
Fib 260	05 08 32.0	–69 00 46	0.99	1248	640	594	1.2	$N_e = 240$
Fib 253	05 08 50.8	–69 03 25	0.68	573	283	107	2.6	Low density limit, low S/N
Fib 259	05 08 53.9	–69 02 33	1.29	363	242	226	1.1	$N_e = 395$ low S/N

the LMC Planetary Nebula (PN) project of Reid and Parker (e.g. Reid & Parker 2006a,b, 2013). AAOmega is a powerful double beam spectrograph (Sharp et al. 2006) that is coupled to the 2dF multi-object fibre spectroscopy system on the AAT (Lewis et al. 2002). Due to the 400 available 2dF fibres it was possible to sacrifice five 2 arcsecond diameter fibres to allocate to the new SNR candidate that happened to be in the field of view of one of the Reid-Parker LMC PN fields. The individual SNR fibres were placed at carefully located positions on the western and eastern edges of the SNR shell as indicated in Fig. 1 with their accurate positions listed in Table 1.

Both the 580V and 1000R gratings were simultaneously employed for the general LMC-PN spectroscopic observations with the 1000R red grating centred at 6850Å and giving coverage from 6300 to 7425Å. This is ideal for medium resolution coverage of the diagnostic Hα, [NII] and [SII] nebular emission lines common to both PN and SNRs and also provides for more accurate radial velocity estimates. The lower resolution 580V blue grating was centred at 4800Å giving coverage from 3700 to 5850Å. The blue data suffered from the effects of extinction and low S/N and was of limited use for the SNR observations.

The AAOmega data was reduced with the standard 2dfdr data reduction pipeline (e.g. Croom et al. 2004). Note that the optical fibres sample both target and superposed sky. Hence it is standard practice to allocate a certain fraction of the 400 2dF fibres to blank sky. This is normally ∼20 fibres as was the case for these observations. However, because the LMC field is of very high stellar density, it was important to carefully manually select decent and representative sky positions across the 2-degree field to avoid stellar or nebulae contamination. An average of these sky spectra are then automatically subtracted from the individual target spectra as part of the 2dfdr data reduction process to provide the sky-subtracted spectra. The resultant 1-D fibre spectra taken at the various points labeled in Fig. 1 are shown in Fig. 3. The measured line ratios are provided in Table 1. All line intensities are relative but the observed line-ratios, because they are so close in wavelength, will not be affected by the lack of a proper flux calibration (difficult for fibres) and so extinction across the limited wavelength range of these emission lines can also be safely ignored.

It is a commonly adopted diagnostic (see Fesen et al. 1985) that an [SII]/Hα ratio >0.5 can separate SNRs from planetary nebula and HII regions as seen and expected in SNRs (e.g Stupar & Parker 2012). It is clear from Table 1 that the observed [SII]/Hα ratio which ranges from 0.6 to 1.29, is strongly in the shocked regime for all fibres, particularly for 2dF fibres 260 and 259 which also happen to be on opposing sides of the optical shell. These ratios all fall well within the SNR domain following the updated diagnostic emission line plots presented by Frew & Parker (2010). Furthermore, the observed [SII]6717/6731Å line ratios also indicate the electron density is close to or in the low density limit as might be expected for such an evolved SNR. Nominal, unphysical, high values (>1.6) for the [S II]6717/6731Å line ratios are observed in the lowest S/N spectra due to the associated larger measurement errors which are also indicated in Table 1.

Table 2. Heliocentric radial velocities estimated from the reduced 1-D 1000R red individual AAOmega fibre spectra as provided by the IRAF emsao package.

2df fibre ID	Radial velocity (km s^{-1})	Error (km s^{-1})	Comments
Fib 238	287.8	6.4	for 2/5 lines
Fib 248	323.0	14.4	for 5/5 lines
Fib 260	275.0	15.1	for 3/5 lines
Fib 253	263.5	13.7	for 3/6 lines
Fib 259	267.8	21.3	for 5/6 lines

The line intensities provided in Table 1 were measured using the IRAF *splot* package. Gaussian profiles were fitted to individual lines, providing the central wavelength, the integrated line flux/intensity, equivalent width and Full Width at Half Maximum (FWHM). The IRAF *emsao* package (Mink & Wyatt 1995) was used to determine the radial velocities for each object as presented in Table 2, clearly showing that the object lies within the LMC. A small 2.5 km/s heliocentric velocity correction has been applied to the measurements. Errors in overall velocities are returned by *emsao* after it estimates weighted averages for all lines measured. These can be seen to increase as the S/N decreases, particularly affecting fibres 259 and 253, whose combined spectra is shown in Fig. 3.

3 DATA ANALYSIS

3.1 Radio

The MIRIAD (Sault et al. 1995) and KARMA (Gooch 1995) software packages were used for reduction and analysis. More information on the observing procedure and other sources observed in this session/project can be found in Bozzetto et al. (2012a,b,c, 2013) and de Horta et al. (2012).

Images were formed using MIRIAD multi-frequency synthesis (Sault & Wieringa 1994) and natural weighting. They

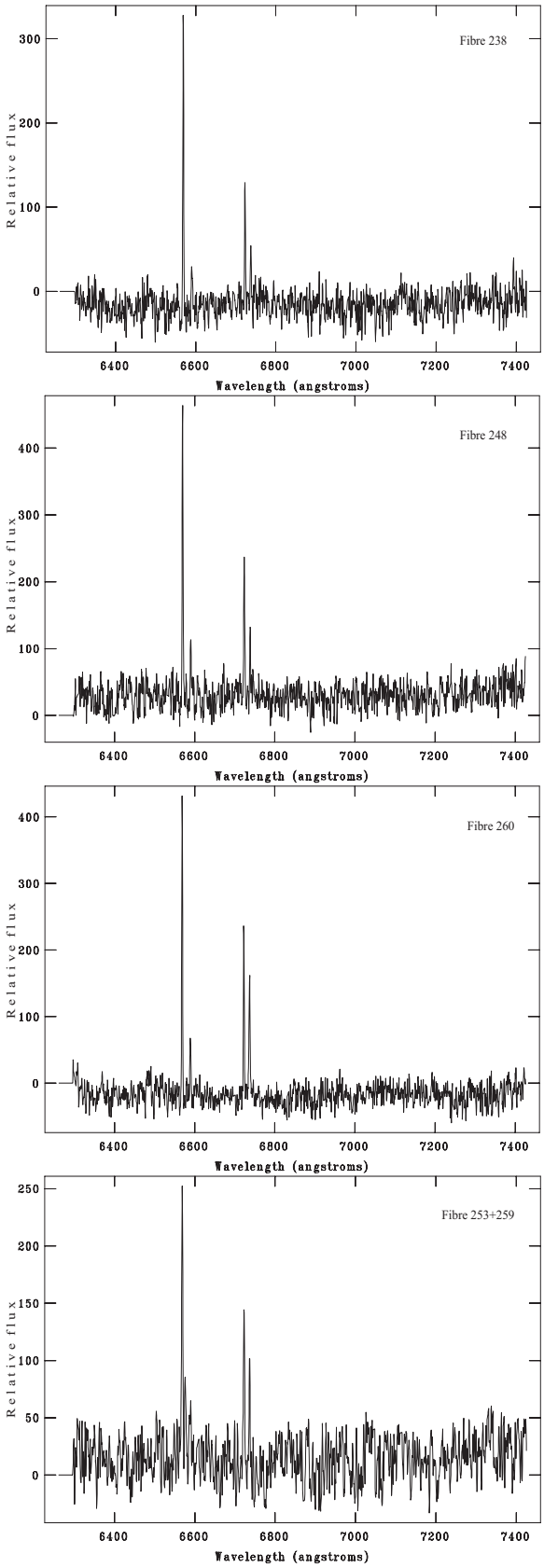

Figure 3. 1000R red grating 1-D 2dF spectra for Fibres 238, 248 and 260 taken on the enhanced western edge and a combined 1-D spectrum from Fibres 253 and 259 taken on the lower surface brightness eastern edge as indicated in Fig. 1.

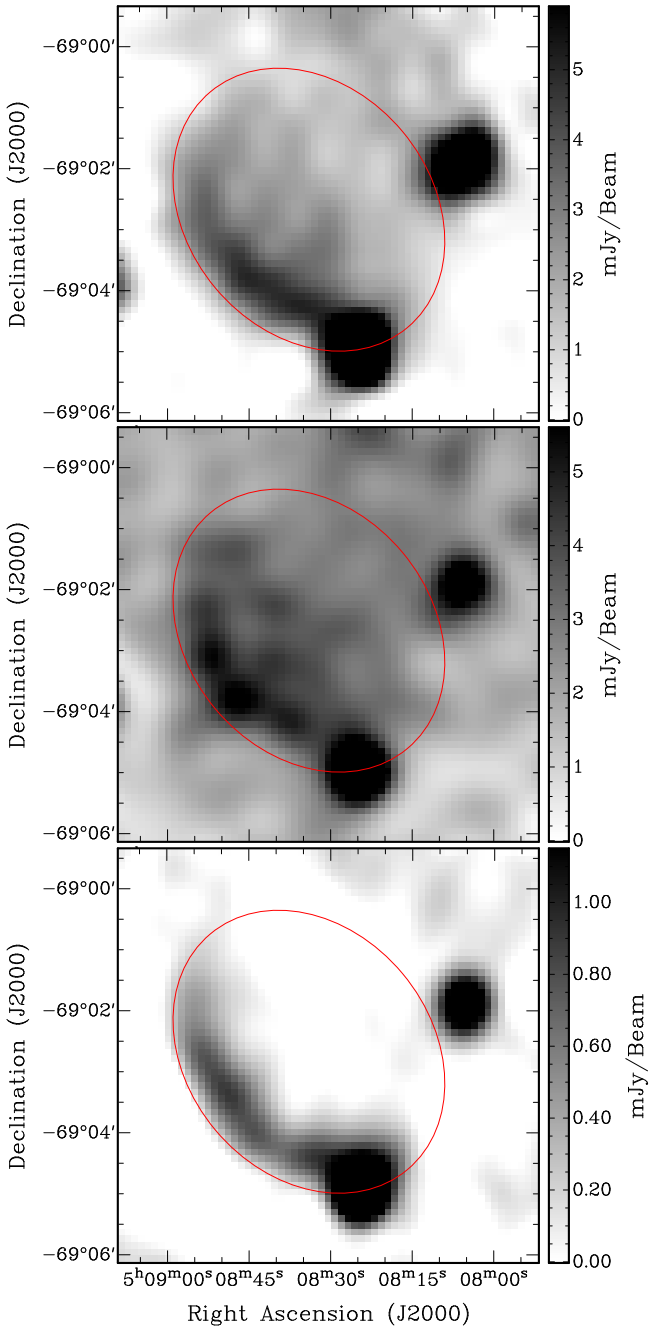

Figure 4. 843 MHz (top), 1400 MHz (middle) and 5500 MHz (bottom) radio-continuum images of MCSNR J0508–6902 with an overlaid ellipse indicating the approximate optical association for this SNR. The side bar quantifies the total intensity in mJy/beam).

were deconvolved using the MFCLEAN and RESTOR algorithms with primary beam correction applied using the LINMOS task. The 6 cm (5500 MHz) ATCA image together with 20 cm (1337 MHz) and 36 cm (843 MHz) mosaic images of MCSNR J0508–6902 are shown in Fig. 4. The resolution of the 6 cm image is $37.7'' \times 25.1''$.

3.2 X-rays

3.2.1 Imaging

We extracted images and exposure maps in three energy bands suited to the analysis of SNRs, whose X-ray emission is mostly thermal: a soft band (0.3–0.7 keV) including strong lines from oxygen; a medium band (0.7–1.1 keV), which includes Fe L-shell lines, as well as the Heα and Lyα lines of Neon; and a hard band (1.1–4.2 keV) comprising lines from Mg, Si, S, Ca, Ar, and, if present, non-thermal continuum.

From the pn detector we selected single and double-pixel events (`PATTERN` = 0 to 4). Below 0.5 keV, only single-pixel events were selected to avoid the higher detector noise contribution from the double-pixel events.. All single to quadruple-pixel (`PATTERN` = 0 to 12) events from the MOS detectors were used. Bad pixels were masked. The detector background (see Sect. 3.2.3) was taken from filter wheel closed (FWC) data[3]. Before it was subtracted from the raw images, we scaled it by a factor estimated from the count rates in the corners of the detectors not exposed to the sky.

We merged MOS and pn data, and combined images from the two *XMM-Newton* observations. We then adaptively smoothed the images, computing Gaussian kernels at each position in order to reach an approximate signal-to-noise ratio of five. The minimum size for the kernels was set to a full width at half maximum (FWHM) of 20″. Smoothed images were finally divided by the vignetted exposure maps.

Combining the final images, we show in Fig. 5 the *XMM-Newton* 'true-color' image of MCSNR J0508–6902, which reveals a striking morphology. A bright central region, dominated by X-rays in the medium band, is surrounded by a fainter and softer shell. The brightness of the interior emission in the 0.7–1.1 keV band, which includes the Fe L-shell lines, suggests that MCSNR J0508–6902 falls into the class of SNRs with central Fe enhancements. Examples of these objects include 0548–70.4 and 0534–69.9 (Hendrick et al. 2003), DEM L238 and DEM L249 (Borkowski et al. 2006), and SNR 0104–72.3 (Lee et al. 2011a, Roper et al., in preparation). Spectral differences between the central region and the shell are analysed in Section 4.3. There is little emission from the object above 1.1 keV. Several point sources are detected outside the boundary of the remnant, which are most likely background objects behind the LMC.

3.2.2 X-ray spectral analysis

We consider only Obs. ID 0690752001 for our spectral analysis. The ∼9 ks of data from Obs. ID 0651880201 can add little to our analysis, as e.g. the faint shell of the remnant is not detected in images from this observation only. Furthermore, using the diagnostic devised by De Luca, Molendi, & Leccardi (2004) [4], we found that the flare–filtered event lists were still heavily contaminated by soft protons.

In addition, only EPIC-pn spectra are considered as the SNR shell is extremely faint in the EPIC-MOS images. Before proceeding with the spectral extraction we generated a vignetting-weighted event list to correct for the effective area variation across our extended source using the SAS task *evigweight*. Only single and double-pixel events (`PATTERN` = 0 to 4) are considered. The extraction area of the central region was defined by enclosing the 0.7–1.1 keV band contours (see Fig. 2) with an ellipse ($\sim 2.8' \times 1.6'$). The shell spectrum was extracted from a $\sim 5'$ diameter region (as determined in Section 4.2), excluding the central extraction region. Backgrounds should ideally be chosen from nearby positions on the detector. However, since the SNR was located close to on-axis and nearby suitable regions were comparatively source and chip-gap heavy, this was not possible. As such, backgrounds were extracted from a source and diffuse emission free region immediately to the northwest of the remnant, further off-axis than the source. This introduces important effects which must be considered in the spectral modelling of the particle-induced background, which is discussed in the forthcoming text. All spectra were rebinned using the FTOOL *grppha*[5] so that each bin contained a minimum of 30 counts. All fits were performed using XSPEC (Arnaud 1996) version 12.7.1 with abundance tables set to those of Wilms et al. (2000), and photoelectric absorption cross-sections set to those of Balucinska-Church & McCammon (1992).

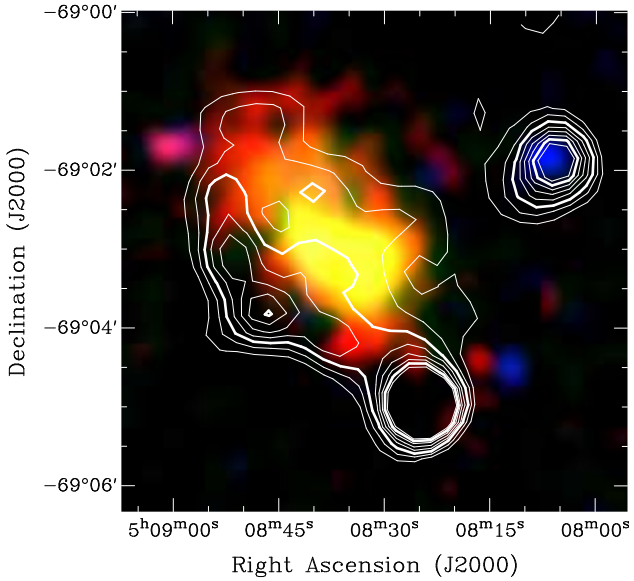

Figure 5. *XMM-Newton* three colour composite (red: 0.3–0.7 keV, green: 0.7–1.1 keV, blue: 1.1–4.2 keV) of MCSNR J0508–6902 smoothed with a Gaussian width of 20″, and overlaid with 1400 MHz radio contours. The contours are from 3σ to 6.5σ in steps of 0.5σ.

3.2.3 X-ray background

Spectral analysis of extended X-ray sources is complicated by the contributions of the X-ray background, comprising particle-induced and astrophysical components. Often, a subtraction of a nearby background region is inappropriate due to the spectral and/or spatial variation of these background components. While the consideration of the X-ray background for bright extended sources may not be so significant, in the case of faint emission (as is the case with the

[3] See `http://xmm2.esac.esa.int/external/xmm_sw_cal/background/filter_closed/index.shtml`
[4] See `http://xmm2.esac.esa.int/external/xmm_sw_cal/background/epic_scripts.shtml`
[5] See `http://heasarc.nasa.gov/lheasoft/ftools/fhelp/grppha.txt`

shell of MCSNR J0508–6902 in particular), the background must be carefully accounted for in order to extract the purest possible information from the source. A commonly used method (see Maggi et al. 2012; for a recent example), is to extract a nearby background spectrum, define a physical model for the background, and simultaneously fit this model to the source and background spectra. We adopt this method for our analysis of MCSNR J0508–6902. A detailed description of our background treatment is given in Appendix A.

3.2.4 MCSNR J0508–6902 emission

Line of sight absorption to MCSNR J0508–6902 consists of a Galactic component ($N_{\rm H\ Gal}$, fixed at 7×10^{20} cm^{-2} as described in Appendix A3) and a foreground LMC component ($N_{\rm H\ LMC,fg}$). These were modelled using photoelectric absorption components with Galactic and LMC abundances, respectively.

Shell emission

We modelled the shell emission using various thermal plasma models appropriate for SNRs. We report here on the results using the standard Sedov model (Borkowski et al. 2001), implemented in XSPEC as *vsedov*. Given the large size of the remnant, the assumption that it is in the Sedov phase is justified. The free parameters of the *vsedov* model are the mean shock temperature (kT_s), postshock electron temperature (kT_e), metal abundances, ionisation timescale (τ_0, the electron density immediately behind the shock front multiplied by the age of the remnant). Due to the relatively poor count statistics, metal abundances for the model were fixed at the average LMC values (0.5 solar, Russell & Dopita 1992a). In the case of MCSNR J0508–6902, fixing the metal abundances at 0.5 solar is quite reasonable as we expect the shell to be dominated by swept-up ISM.

Interior emission

Fits of the central spectrum are complicated by the fact that we must consider both the interior Fe-rich gas and the emission from the shell overlapping this region. To account for the shell emission we included a *vsedov* component in the fits to the central spectrum with the shell kT_s ($= kT_e$) and τ_0 fixed to the best-fit values determined from fits to the shell spectrum (see above). For the interior emission itself we considered several thermal plasma models, which are discussed in detail in Section 4.3.2.

4 RESULTS

4.1 Radio

This remnant exhibits a filled-in shell morphology (at 20 cm) centred at RA(J2000)=$05^h08^m33.7^s$ and DEC(J2000)=–$69°02'33''$. There are two unrelated background sources in the field, one in the south (RA(J2000)=$05^h07^m57.7^s$, DEC(J2000)=–$69°03'59.49''$), and the other to the west (RA(J2000)=$05^h08^m06.94^s$, DEC(J2000)=–$69°01'51.2''$) (Fig. 4). At lower radio frequencies in this study (843 & 1400 MHz), the emission of the SNR is fairly uniform across the remnant with significant limb brightening in the south-east. As we move to higher frequencies ($\geqslant$5500 MHz), the remnant maintains this south-eastern limb but loses the shell emission of the remnant until we get to 9000 MHz, at which point all emission from the SNR is lost.

Table 3. Integrated flux densities of MCSNR J0508–6902 measured in this study.

λ (cm)	ν (MHz)	R.M.S (mJy)	Beam Size ($''$)	$S_{\rm Total}$ (mJy)	$\Delta S_{\rm Total}$ (mJy)
20	1377	0.7	40.0×40.0	88	15
6	4800	1.0	35.0×35.0	41	10
36	843	0.4	46.4×43.0	59	6
20	1377	0.7	40.0×40.0	51	5
6	4800	—	33.0×33.0	19	2

The top two flux density measurements include a zero-spacing measurement, whereas the lower three measurements do not.

The large extent of MCSNR J0508–6902 made a spectral energy distribution (SED) estimate difficult, as observations using an interferometer suffer from missing zero-spacings (which are responsible for large scale, extended emission), and therefore, missing flux. Because of this, we take two different sets of flux density measurements to estimate the SED. The first set of measurements came from mosaic images (20 cm from Hughes et al. 2007 and 6 cm from Dickel et al. 2010) which include a zero-spacing observation. The second set (which do not use a zero-spacing observation) include the two aforementioned mosaics before the zero-spacing (Parkes) observation were added, in addition to a 36 cm measurement from the Molonglo Synthesis Telescope (MOST) mosaic image (as described in Mills et al. 1984). The values of these flux density measurements are reported in Table 3, and then used to produce a spectral index graph (Fig. 6). The spectral indices for both the zero-spacing inclusive ($\alpha = -0.62 \pm 0.34$) and the non inclusive ($\alpha = 0.69 \pm 0.12$) are quite similar. We note however, as u–v coverage is a function of distance and frequency, the 6 cm measurement without the short-spacing is missing more extended emission than those at lower frequencies. Therefore, we would expect a flatter spectral index than we see from these measurements (and potentially closer to what we see in the zero-spacing measurements).

There was no reliable detection in the Q or U intensity parameters associated with this object, implying a lack of polarisation at higher radio frequencies (5500 & 9000 MHz). Without these detections, we were unable to determine the Faraday rotation and therefore cannot deduce the magnetic field strength. As an alternative however, we were able to estimate the magnetic field strength for this SNR based on the equipartition formula as given in Arbutina et al. (2012). This formula is based on the Bell (1978) diffuse shock acceleration (DSA) theory. We use the spectral index which is inclusive of zero-spacing measurements ($\alpha = -0.62$) for this equipartition measurement. We find the average equipartition field over the whole shell of SNR MCSNR J0508–6902 to be $\sim$28 μG (this value is typical for the compressed interstellar magnetic field by the strong shock wave of an older SNR), and an estimated minimum SN explosion energy of

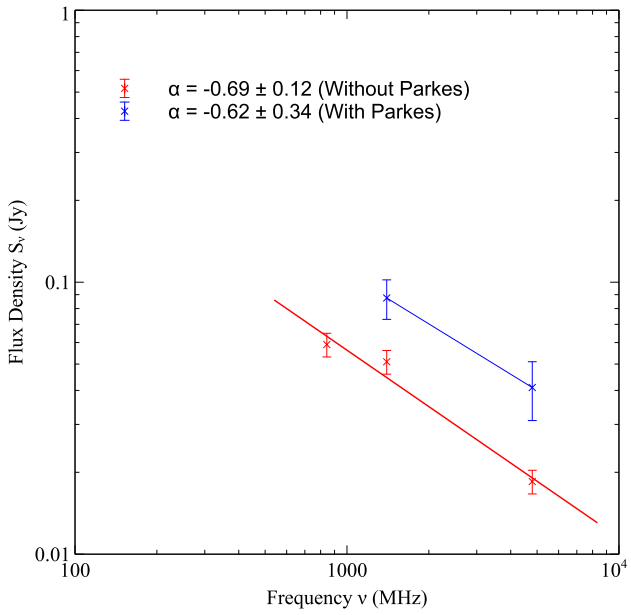

Figure 6. Radio-continuum spectrum of MCSNR J0508–6902.

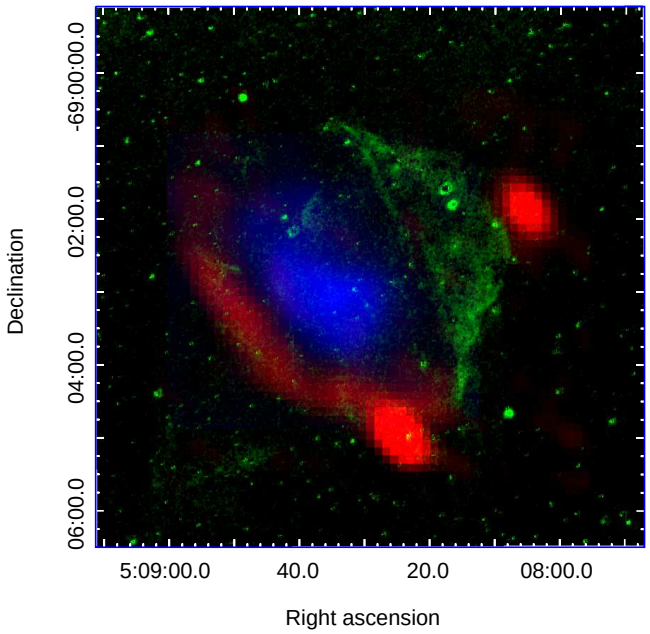

Figure 7. Radio (5500 MHz) [red], Optical (Hα) [green] & X-ray (0.7–1.1 keV) [blue] emission of MCSNR J0508–6902.

$E_{min} = 1.6\times10^{50}$ ergs (see Arbutina et al. (2012); and corresponding calculator[6]).

From the position of MCSNR J0508–6902 at the surface brightness to diameter (Σ - D) diagram ((D, Σ) = (65.5 pc, 1.4×10^{-21} W m^{-2} Hz^{-1} sr^{-1})) by Berezhko & Völk (2004), we can estimate that MCSNR J0508–6902 is likely to be an older SNR probably in the transition phase between Sedov and radiative phases of evolution.

4.2 Multifrequency Morphology

The morphology of the soft X-ray emission (0.3–0.7 keV) of MCSNR J0508–6902 is similar to that of the 20 cm radio-continuum emission (Fig. 5), filling out the shell of the remnant. X-ray emission in the medium band (0.7–1.1 keV) appears to be encased within the radio and optical emission, making the central location of this emission evident.

In the MCELS combined RGB Hα, [O III] and [S II] optical image we can see an association between the [O III] emission and radio emission (Fig. 2) where the [O III] emission perfectly fits within the confines of the radio emission along the south-eastern limb of the remnant and then extending in the northern region to further complete the ellipse ring structure of the remnant. On the other hand, the Hα and [S II] emission located in the north-western regions of the remnant show no association with the radio-continuum emission at any frequency, nor with the X-ray emission (Fig. 2). The Hα and [S II] emission in the north-west is significantly stronger when compared to the faint [O III] emission. Strangely enough, they almost perfectly complement the [O III] emission in creating an ellipse ring morphology. This morphology is similar to that of LMC SNR J0453–6829 (Haberl et al. 2012).

[6] The calculator is available on `http://poincare.matf.bg.ac.rs/~arbo/eqp/`

Due to the higher resolution of Hα images from the deep Hα survey of the central 25 sq. degrees of the LMC by Reid & Parker (2006a) (Fig. 1 & 7), we are able to see a complete optical shell which perfectly follows the radio emission in the south-east. The enhanced optical emission seen in this image towards the north-west suggests propagation of the shock front into the slightly higher density ISM, compared with somewhat lower density ISM on the south-east side. Separate fragmented Hα filaments inside the shell are common in optical observations (as well as in radio), as Hα emission is dominant where the blast propagates into dense, cooler regions.

X-ray, radio and optical images were combined to estimate the extent of this object. To do so, we created an annotation file which comprised of an ellipse that followed the outer emission from these combined images. We deduce an extent of $304'' \times 234'' \pm 4''$ ($74\times57\pm1$ pc), which places this remnant amongst the 20% largest SNRs in the LMC (Badenes et al. 2010).

To gain an understanding of the environment in which the remnant resides, we use an image from the NANTEN molecular cloud survey by Kawamura et al. (2009), and another from the higher resolution Magellanic Mopra Assessment (MAGMA) survey by Wong et al. (2011). From these images (Fig. 8), it appears that the remnant is confined within the CO emission, elongated and stretching into the less dense region towards the north-east. However, this may be a projection effect as there is no reason to believe that the SNR is at the same distance as the molecular cloud. If it is though, perhaps the expansion could have been stopped by the cloud but some of it got broken up and ionized by the radiation from the explosion, giving rise to the asymmetry. MCSNR J0508–6902 was also found to be located at the rim of the supergiant HI shell SGS 5, identified by Kim et al. (1999). We recreated their HI channel maps of

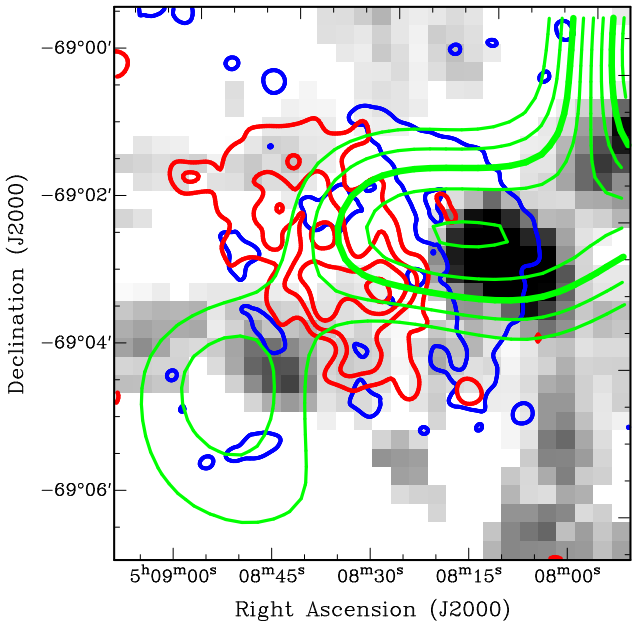

Figure 8. *XMM-Newton* (0.3–0.7 keV; red) and Hα (blue) contours of MCSNR J0508–6902 overlaid on NANTEN molecular cloud contours (green) and MAGMA molecular cloud grayscale intensity image, showing the association between the denser environment and the emission from the remnant.

SGS 5 (their Fig. 5e) at the position of MCSNR J0508–6902 using ATCA-Parkes 21 cm observations from the HI Magellanic Cloud Survey[7], shown in Fig. 9. The ATCA and Parkes observations are outlined in Kim et al. (1998) and Kim et al. (2003), respectively. By definition, HI supergiant shells have radii that exceed the neutral gas scale height of the LMC (∼180 pc) and, thus, have blown out both sides of the disk, effectively creating a cylindrical wall of HI gas. Indeed, the molecular cloud shown in Fig. 8 is most likely located, and may have been formed in SGS 5 (Dawson et al. 2013). The extent of SGS 5 through the LMC disk, increases the likelihood of an interaction with MCSNR J0508–6902 and can provide the density gradient required to explain the asymmetric optical and radio emission.

Because of the bright interior X-ray emission, this remnant could be suggested to be a member of the mixed–morphology SNR (MMSNR, Rho & Petre 1998, Lazendic & Slane 2006). These remnants shows indications for interactions with molecular clouds and often show associated OH maser emission. These features led some authors to conclude to a core-collapse origin for these type of SNRs (e.g. Micelli 2011). In the case of MCSNR J0508–6902, although there is some evidence of interaction with a molecular cloud, we clearly favour a type Ia SN progenitor (see Sect. 4.3.2). We note that other type Ia SNRs have been found in a molecular cloud/star forming environment (e.g. Lewis et al. 2003, Lee et al. 2011b). In addition, over-ionised (i.e. recombining) plasma have been found recently in several Galactic MMSNRs (Yamaguchi et al. 2009, Ohnishi et al. 2011, Yamauchi et al. 2013), while this feature is absent in the spectrum of MCSNR J0508-6902. Finally, we note that this classification has only been applied to Galactic remnants and not to the (usually Fe-rich) 'centrally-peaked in X-rays' SNRs in the Magellanic Clouds (see Sect. 5 and references therein).

[7] Available at `http://www.atnf.csiro.au/research/HI/mc/`

Table 4. Results of the spectral fits. For the *vsedov* model, the postshock mean temperature and postshock electron temperature were set to be the same ($kT_s = kT_e = kT$) and the abundance is set to that of the LMC (0.5 solar). The EM and $L_{\rm X,0.2-10\ keV}$ values for the shell were calculated for the *total* shell (i.e., central and shell region). The ranges in parentheses represent the 90% confidence intervals on the parameters.

Shell emission: *vsedov* model	
Fit parameter/result	Value
kT (keV)	0.41 (0.35–0.46)
τ (10^{12} s cm^{-3})	2.70 (1.73–6.92)
χ^2/ν	267.08/219
EM (10^{57} cm^{-3})	4.75 (2.54–7.22)
$L_{\rm X,0.2-10\ keV}$ (10^{34} erg s^{-1})	5.1
Interior emission: pure heavy element *vapec* models	
Fit parameter	Value
$kT_{\rm Fe,O}$ (keV)	0.78 (0.75–0.81)
χ^2/ν	66.49/64
$n_e n_{Fe} V$ (10^{53} cm^{-3})	0.58 (0.54–0.61)
$n_e n_O V$ (10^{53} cm^{-3})	2.99 (0–9.96)
$L_{\rm X,0.2-10\ keV}$ (10^{34} erg s^{-1})	2.8

4.3 X-ray emission of MCSNR J0508–6902

4.3.1 Shell emission

As stated in Section 3.2.4, we modelled $N_{\rm H\ LMC,fg}$ using a photoelectric absorption model with LMC abundances. However, $N_{\rm H\ LMC,fg}$ consistently tended to zero, with upper 90% confidence intervals for this parameter of $\sim 8 \times 10^{20}$ cm^{-2} for all fits. Thus, we fixed $N_{\rm H\ LMC,fg}$ at 0. Initial shell fits with the *vsedov* model resulted in best-fit values for kT_s and kT_e to be equal within their 90% confidence intervals and, thus, kT_s and kT_e were constrained to be the same. Indeed, we should expect that evolved SNRs are close to ion-electron temperature equilibrium (Borkowski et al. 2001).

The results of the spectral fits to the shell and central regions of MCSNR J0508–6902 are given in Table 4. The *vsedov* model provides an acceptable fit to the shell spectrum with a reduced χ^2 of 1.21. The best-fit temperature to the shell emission of $kT_s = kT_e = 0.41(^{+0.05}_{-0.06})$ keV is consistent with other large LMC SNRs (see Williams et al. 2004, Grondin et al. 2012; for example), as well as DEM L238 and DEM L249 from Borkowski et al. (2006). The high value of τ_0 ($\sim 10^{12}$ s cm^{-3}) indicates that the plasma is in ionisation equilibrium. From the shell component in the fits to the central spectra, we determined that 13-28% of the *total* shell emission is contributing to the central spectrum. The absorption corrected X-ray luminosity ($L_{\rm X}$) of the shell in the 0.2–10 keV range was found to be $\sim 5 \times 10^{34}$ erg s^{-1}.

Using our fit results we can further estimate physical parameters of the SNR using the Sedov dynamical model (see Sasaki et al. 2004; for example). We know that

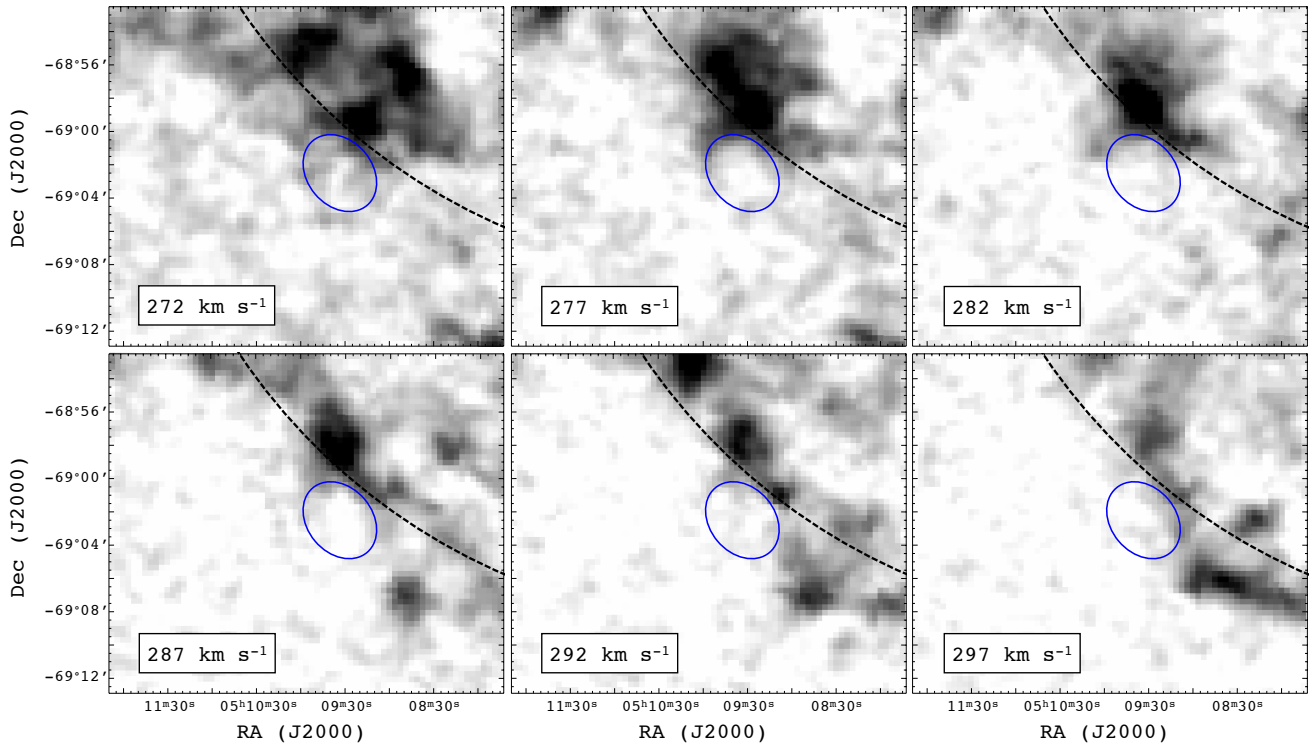

Figure 9. HI channel maps of SGS 5 in the region of MCSNR J0508–6902. The dimensions of the SNR are shown by the blue ellipses. The black dashed lines mark the approximate SGS 5 dimensions as determined by Kim et al. (1999). The heliocentric velocities are also indicated. A density gradient across MCSNR J0508–6902 due to SGS 5 is evident in each channel.

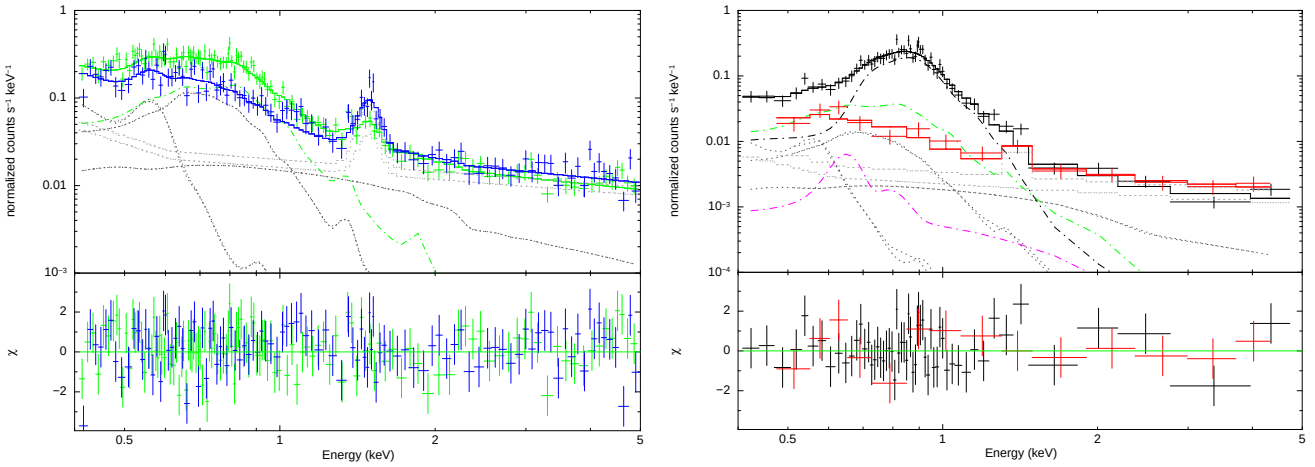

Figure 10. *XMM-Newton* spectral fits to MCSNR J0508–6902 shell (left) and central spectra (right) and associated backgrounds. The shell spectrum is shown in green, the shell background in blue, the central spectrum in black, and the central background in red, with the best-fit model to each represented by the solid lines of matching colour. The astrophysical background components are indicated by the dark grey dotted lines in each plot. The particle induced background components are indicated by the light grey dotted lines. The green dash-dot line in each spectrum represents emission from the shell. The black and magenta dash-dot lines in the central spectrum show the pure Fe component and the pure O component, respectively.

MCSNR J0508–6902 is not spherically symmetric since the semi-major and semi-minor axes are 37 pc and 28.5 pc, respectively. Taking these semi-major and semi-minor axes as the first and second semi-principal axes of an ellipsoid describing MCSNR J0508–6902, and assuming that the third semi-principle axis is in the range 28.5-37 pc, we determined the volume (V) limits for the remnant and their corresponding effective radii ($R_{\rm eff}$) to be $(3.7 - 4.8) \times 10^{60}$ cm^3 and 31.1–33.9 pc, respectively. In the following calculations we evaluate the physical parameters of the remnant at these volume and effective radii limits, and determine the resulting range for each parameter.

The X-ray temperature corresponds to a shock velocity

$$v_s = \left(\frac{16kT_s}{3\mu}\right)^{0.5}, \quad (1)$$

where kT_s is the postshock temperature and μ is the mean mass per free particle. For a fully ionised plasma with LMC abundances, $\mu = 0.61$, resulting in a shock velocity of $v_s = 572(\pm36)$ km s^{-1}. The age of the remnant can now be determined from the similarity solution:

$$v_s = \frac{2R}{5t}, \quad (2)$$

where $R = R_{\rm eff}$ and t is the age of the remnant. This gives an age range of $20 - 25$ kyr. The preshock H density ($n_{\rm H,0}$) in front of the blast wave can be determined from the emission measure (EM, see Table 4). Evaluating the emission integral over the Sedov solution using the approximation for the radial density distribution of Kahn (1975) gives

$$\int n_e n_{\rm H} dV = EM = 2.07 \left(\frac{n_e}{n_{\rm H}}\right) n_{\rm H,0}^2 V, \quad (3)$$

where $n_{\rm e}$ and $n_{\rm H}$ are electron and hydrogen densities, respectively, V is the volume (e.g., Hamilton et al. 1983). Taking $n_e/n_{\rm H} = 1.21$ and the determined range of volumes, this equation yields $n_{\rm H,0} = (1.5 - 2.8) \times 10^{-2}$ cm^{-3}. Since the preshock density of nuclei is given as $n_0 \sim 1.1 n_{\rm H,0}$, it follows that $n_0 = (1.7 - 3.1) \times 10^{-2}$ cm^{-3}. Hence, the SNR is expanding into a fairly rarified environment. The initial explosion energy (E_0) can be determined from the equation:

$$R = \left(\frac{2.02 E_0 t^2}{\mu_n n_0}\right)^{1/5}, \quad (4)$$

where μ_n is the mean mass per nucleus ($= 1.4 m_p$). This results in an initial explosion energy in the range $(0.37 - 0.75) \times 10^{51}$ erg which is less than the canonical value of 10^{51} erg but consistent with several Type Ia SNRs in the LMC (see Hendrick et al. 2003; for example). The swept-up mass contained in the shell is given simply by $M = V \mu_n n_0$, which is evaluated to $(32 - 62)$ M$_\odot$. This large amount of swept-up material supports our original assumption that MCSNR J0508–6902 is into the Sedov phase of its evolution. All the derived parameters of MCSNR J0508–6902 are summarised in Table 5. Using the determined values of t and n_0 we estimated the expected ionisation age for the remnant, given as $4.8 n_{\rm H,0} t$, to be in the range $(5.3 - 9.2) \times 10^{10}$ cm^{-3} s. This is significantly less than the ionisation age determined from the spectral fits with the Sedov model. Given this inconsistency, it is likely that the Sedov model may not be strictly applicable to MCSNR J0508–6902. Several other remnants exhibit a similar discrepancy between measured and expected ionisation timescales. Hughes et al. (1998) and van der Heyden et al. (2003) observed this for candidate CC SNRs in the LMC and SMC, respectively. Hughes et al. (1998) suggest the explanation to be that the remnants initially expand into a low density cavity in the ISM, likely due to the massive stellar wind. The remnant rapidly reaches the wall of the cavity where it meets the denser material, slows down, and emits X-rays. This scenario represents a deviation from the standard Sedov model of a remnant expanding into a uniform ambient medium and can account for the discrepancy in the measured and expected ionisation ages. The problem with this scenario as an explanation for MCSNR J0508–6902 is that a high mass stellar wind is required to alter the ambient ISM in such a manner which is likely not the case for MCSNR J0508–6902. Borkowski et al. (2006) also observe such a discrepancy for DEM L238, a Type Ia remnant. They suggest that their derived ambient ISM density may be underestimated resulting in the ionisation parameter discrepancy. It is unclear as to the reason for the observed discrepancy in MCSNR J0508–6902, however, it is most likely the case that it is due to some density variation in the ambient ISM causing a deviation from the standard Sedov picture. The optical and radio morphologies discussed in Section 4.2 suggest that MCSNR J0508–6902 is evolving into a denser medium in the west. The higher $n_{\rm H,0}$ value in the west of the remnant will result in an increased ionisation age in the west as compared to the east. This may explain the observed ionisation parameter discrepancy. However, in such a picture we would expect variation of the X-ray emission in this direction. Unfortunately, given the already low count statistics, an analysis of spatio-spectral variation is not really feasible. In any case, because of the discrepancy between the measured and expected ionisation parameters, the SNR properties derived from the Sedov dynamical model are somewhat uncertain.

Table 5. Physical properties of MCSNR J0508–6902 derived from the Sedov model

n_0 (10^{-2} cm^{-3})	v_s km s^{-1}	t (kyr)	M (M$_\odot$)	E_0 (10^{51} erg)
1.7–3.1	536 – 608	20–25	32 – 62	0.37 - 0.75

4.3.2 Interior emission

We initially fitted the interior emission with a *vapec* model at LMC abundances. However, this resulted in a very poor fit (red. $\chi^2 > 2$) with large residuals at ~ 0.9 keV due to the Fe L-shell emission lines. Thus, we freed the Fe abundance and re-performed the fit, resulting in a substantially improved fit with $kT = 0.76$ $(0.73 - 0.79)$ keV, $Z_{\rm Fe} > 2.01$ $Z/{\rm Z}_\odot$, and red. $\chi^2 = 1.08$. The lower limit for the Fe abundance is ~ 4 times higher than the average LMC value, clearly indicating an overabundance of Fe in the central region, most likely due to Fe-rich ejecta being heated by the reverse shock. Allowing other metal abundances to vary (e.g. O) did not improve the fits and were very poorly constrained.

A more realistic model can be applied assuming that the interior gas consists of ejecta only. Hence, we applied thermal plasma models, representative of pure heavy-element plasmas (see Kosenko et al. 2010; for example). We performed trial fits with collisional ionisation equilibrium (CIE) models and non-equilibrium ionisation (NEI) models representing the pure metal plasmas and found that, in both cases, a Fe plasma was required to fit the spectrum of the interior emission with a minimal pure O contribution. The CIE models provided acceptable fits to the spectra (reduced $\chi^2 \approx 1$). Similar quality fits were achieved with NEI models with the formal best-fit ionisation timescales determined as $\sim 10^{13}$ s cm^{-3}, suggestive of a plasma in CIE.

However, no constraints could be placed on these values. Given the quality of the trial fits with the CIE models, the interior plasma is suggested to be close to or in CIE. Hence, we model this emission using the *vapec* model in XSPEC. Initial fits showed that the temperature of the O component was not well constrained. Hence, as in Hughes et al. (2003), we simplified the model by assuming the O and Fe to be co-spatial and constrained their temperatures to be the same. This yielded a best-fit $kT = 0.78^{+0.03}_{-0.03}$ keV. In our spectral fits we found that Fe dominates the interior emission with O having little or no contribution to the spectrum. Indeed, the normalisation of the O component was pegged at zero, demonstrating that it is formally not required. However, we keep the component in the spectral model as the upper limit to the O contribution can allow us to at least determine the maximal O/Fe ratio (see below). We reiterate that the interior plasma is likely in or close to CIE due to the quality of the *vapec* model fit (reduced $\chi^2 \approx 1$, see Table 4). The $L_{\rm X}$ of the interior gas in the 0.2–10 keV range was found to be $\sim 2.8\times10^{34}$ erg s^{-1}.

It is possible to identify the likely SN mechanism responsible for MCSNR J0508–6902 by assessing the O/Fe ratio of the interior region. From the SN nucleosynthesis yields of Iwamoto et al. (1999), the O/Fe ratio is expected to be 0.3–0.7 by number for Type Ia events and $\sim$ 70 for core-collapse events. We estimated the maximum allowed O/Fe ratio for MCSNR J0508–6902 using a χ^2 contour plot produced for the Fe and O normalisation parameters. This yielded a maximum ratio of < 21 at the 90% confidence level, slightly higher than the LMC value of 13.2 (Russell & Dopita 1992b). We stress that this upper limit is based on the rather poorly constrained, formally not required O component in the spectral fits. However, it does rule out a CC scenario, indicating MCSNR J0508–6902 likely resulted from a Type Ia explosion. Another diagnostic for the SN type, is the mass of Fe produced. This can be estimated using Equation 2 of Kosenko et al. (2010), adapted for Fe. We split this equation into terms which are easily determined from the fit results, given as

$$M_{\rm Fe} = (V_{\rm Fe} EM_{\rm Fe})^{0.5} (n_{\rm e}/n_{\rm Fe})^{-0.5} m_{\rm U} A_{\rm Fe} \quad (5)$$

where $V_{\rm Fe}$ is the volume occupied by the Fe, $EM_{\rm Fe} = n_e n_{Fe} V$ is the emission measure of the Fe gas, $n_{\rm e}/n_{\rm Fe}$ is the electron to Fe-ion ratio, $m_{\rm U}$ is the atomic mass unit, and $A_{\rm Fe}$ is the atomic mass of Fe. $V_{\rm Fe}$ is determined from the dimensions of the central region ($1.4' \times 0.8'$) and assuming an ellipsoidal morphology with a third semi-axis equal to the mean of the semi-major and semi-minor axes ($1.1'$). If the actual morphology is oblate or prolate, the volume would be 13% higher or lower, respectively. $EM_{\rm Fe}$ is obtained from the normalisation of the Fe component and is listed in Table 4. We must estimate the $n_{\rm e}/n_{\rm Fe}$ ratio. As discussed in Hughes et al. (2003), there are two plausible scenarios for the number of electrons per Fe ion, depending on the level of admixture of H in the ejecta. If there is no H, then the number of free electrons per Fe ion only depends on the average ionisation state of the each metal contributing electrons. We do not consider the contribution of electrons by the minimal O content of the interior region. For a plasma in CIE at $kT = 0.78$ keV ($\log T = 6.95$), the average ionisation is 18.3 for Fe (Shull & van Steenberg 1982). Then, from Equation 5, the Fe mass is in the range 1.6–1.8 $M_\odot$ for the pure heavy element scenario. The second case proposed by Hughes et al. (2003) is that a similar mass of H is mixed into the metal rich ejecta. Therefore, the number density of Fe over H is 1/56, and the average number of electrons per Fe ion is 74.3. Thus, from Eq. 5 we have an Fe mass range of 0.8–0.9 $M_\odot$ if there is a comparable mass of H to Fe in the ejecta. The former case gives a value somewhat too high for the explosion of a white dwarf, the latter value being typical of a Type Ia yield. However, the ejecta might be clumpy, with a filling factor of ~ 0.4 (see Kosenko et al. 2010; and references therein), in which case the Fe content reduces by a factor of $\sqrt{0.4} \approx 0.63$ giving 1.0–1.1 $M_\odot$ and 0.5–0.6 $M_\odot$ for the pure Fe and Fe+H mixture cases, respectively. The large mass of Fe present in the interior further supports a Type Ia progenitor for MCSNR J0508–6902.

5 DISCUSSION

The X-ray emission from MCSNR J0508–6902 is notable due to the Fe-rich gas in the interior of the remnant, which is typically indicative of a Type Ia origin (Vink 2012; and references therein). MCSNR J0508–6902 is not the only SNR to exhibit such a feature, with a number of SNRs also characterised by central Fe enhancements in both the LMC: 0454–67.2 (Seward et al. 2006); 0548–70.4 and 0534–69.9 (Hendrick et al. 2003); DEM L316A (Nishiuchi et al. 2001, Williams & Chu 2005); DEM L238 and DEM L249 (Borkowski et al. 2006); and the SMC: DEM S128, IKT 5, and IKT 25 (van der Heyden et al. 2004, Filipović et al. 2000, 2008); SNR 0104–72.3 (Lee et al. 2011a). Of these, DEM L316A, DEM L238, and DEM L239 are most similar to MCSNR J0508–6902 as, not only is a faint shell detected surrounding the interior Fe-rich gas, but also the Fe-rich gas is in CIE. However, as argued by Borkowski et al. (2006), it is likely that many more SNRs fall into this category, only their shells are so faint as to be undetectable by *XMM-Newton*. DEM S128 (Filipović et al. 2000) and IKT 5 (Roper et al., in preparation) are examples of such SNRs with an Fe-rich gas in CIE but no detected shell. The X-ray structure of such SNRs presents a problem for standard Type Ia models (Dwarkadas & Chevalier 1998, Badenes et al. 2003, 2005, 2006). Assuming that the SN ejecta have expanded in a uniform ambient ISM, and we know from the X-ray analysis that the ambient density is quite low ($\sim 10^{-2}$ cm^{-3}), then, under the standard Type Ia models, the central Fe-rich gas should be of low density and the ionisation times are short, which are not observed. Borkowski et al. (2006) demonstrate these scenarios using 1D hydrodynamic simulations using the model of Dwarkadas & Chevalier (1998) and find consistency with the results of Badenes et al. (2003, 2005, 2006).

To explain the X-ray properties of DEM L238 and DEM L249, Borkowski et al. (2006) argue that, rather than the SNR expanding into an ideal environment of uniform density, the structure of the ejecta and/or the uniformity of the ambient ISM deviates from the standard Type Ia models. The best candidates for such a scenario are the 'prompt' Type Ia explosions (Mannucci et al. 2006, Sullivan et al. 2006, Aubourg et al. 2008). These

'prompt' events are produced by relatively massive stars ($\sim 3.5 - 8$ M$_\odot$, Aubourg et al. 2008) and are capable of increasing the circumstellar medium (CSM) density via ejection of their stellar envelope prior to the supernova event. Alternatively, the SN ejecta themselves could have stripped the companion of its envelope (Marietta et al. 2000). As stated by Borkowski et al. (2006), at late stages of SNR evolution, the Fe-contaminated envelope would be evident as dense Fe-rich gas close to the centre of the SNR. Ultimately, this is simply a plausible scenario to explain the observed X-ray morphologies and spectra of MCSNR J0508–6902 and similar remnants. However, it is clear that the standard Type Ia model fails to explain the properties of these SNRs and some mechanism for a pre-explosion increase in the CSM density is essential. Secondary evidence to support the 'prompt' explosion scenario can be found in the stellar content and star-formation history (SFH) of the region, further supporting the scenario described above.

To understand the type of stellar environment the progenitor of this SNR came from, we make use of data from the Magellanic Cloud Photometric Survey (MCPS Zaritsky et al. 2004) to construct colour–magnitude diagrams (CMDs) and identify blue stars more massive than $\sim$8 M$_\odot$ within a 100 pc ($\sim$6.9′) radius of MCSNR J0508–6902. This allows us to see the prevalence of early-type stars close to the remnant. In the case of MCSNR J0508–6902, there are not many early-type stars close to the remnant (16), which is far fewer than around DEM L205 (Maggi et al. 2012), where we found 142 stars and concluded to a CC-SN origin, and more similar to SNRs such as SNR J0530–7007 (de Horta et al. 2012) with 13 early-type stars or J0527–7104 (Kavanagh et al. 2013) with 5 such stars.

Studying the SFH in the neighbourhood of MCSNR J0508–6902 (see Fig. 11) as derived from the map of Harris & Zaritsky (2009), we see modest levels of star-formation ($\sim 10^{-3}$ M$_\odot$/yr) peaking 12 Myr ago (accounting for the presence of several early-type stars as described in the previous paragraph), 100 Myr ago, and extending back from 250 Myr to 1 Gyr. The peak at a lookback time of 100 Myr is consistent with a relatively young progenitor able to produce dense CSM, but we cannot rule out an older progenitor. A 'delayed' progenitor older than $\sim$2.4 Gyr (e.g. Maoz et al. 2011) is however less likely.

Borkowski et al. (2006) discussed the possibility of the iron-rich DEM L238 and DEM L249 remnants to be those of sub-luminous SN2002cx-like Type Ia SNe. Recent studies of this peculiar class of SNe (Jordan et al. 2012, Foley et al. 2013, Kromer et al. 2013) interpret these SNe as failed-detonations of a white dwarf, which leads to relatively low initial kinetic energies ($\sim 0.13 \times 10^{51}$ erg) and ejecta masses ($\lesssim$ 0.5 M$_\odot$). Our estimates of E_0 and $M_{\rm Fe}$ are at odds with these properties, suggesting that MCSNR J0508–6902 is likely not the remnant of a failed-detonation SN. Further studies of centrally iron-rich SNRs and discovery of new members of that class is highly desirable to address the questions of what are the progenitors of these objects, and if and how they differ from the remnants of 'standard' Type Ia SNe.

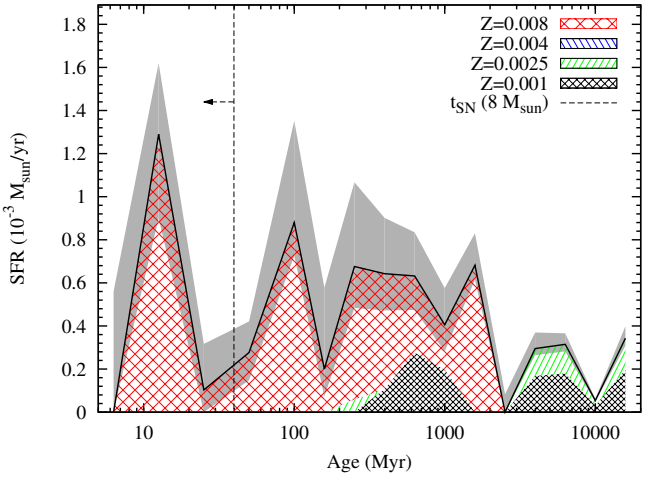

Figure 11. Star-formation history around MCSNR J0508–6902. We show the star-formation rate (SFR) as a function of lookback time for different metallicity bins, using the map of Harris & Zaritsky (2009). The gray shading denotes the uncertainties on the total SFR. The time scale for a core-collapse SN ($\lesssim$ 40 Myr) to explode is indicated by the dashed line.

6 SUMMARY

We have undertaken a detailed multi-wavelength study of a new LMC SNR candidate, MCSNR J0508–6902, using radio, X-ray and optical data (both imaging and spectroscopy) that confirm we have uncovered a new LMC SNR. With this analysis we infer that MCSNR J0508–6902 is an evolved remnant, with a large size of $\sim$74×57 pc. We estimate the magnetic field strength to be $\sim$28 μG and an age of $\sim 20 - 25$ kyr. Based on the determined O/Fe ratio of the interior gas and the mass of Fe ejecta, we conclude that this remnant is of a thermonuclear SN. It is most likely that this remnant was the result of a 'prompt' Type Ia event, sharing similar properties to various other prompt Ia LMC SNRs.

ACKNOWLEDGEMENTS

We used the KARMA and MIRIAD software package developed by the ATNF. The Australia Telescope Compact Array is part of the Australia Telescope which is funded by the Commonwealth of Australia for operation as a National Facility managed by CSIRO. We thank the Magellanic Clouds Emission Line Survey (MCELS) team for access to the optical images. We thank Dr. David Frew at Macquarie University for useful discussions. This research is supported by the Ministry of Education and Science of the Republic of Serbia through project No. 176005. M.S. acknowledges support by the Deutsche Forschungsgemeinschaft through the Emmy Noether Research Grant SA 2131/1. P. M. and P. K. acknowledge support from the BMWi/DLR grants FKZ 50 OR 1201 and 50 OR 1209, respectively.

REFERENCES

Arbutina B., Urošević D., Andjelić M. M., Pavlović M. Z., Vukotić B., 2012, ApJ, 746, 79

Arnaud K. A., 1996, in Jacoby G. H., Barnes J., eds, Astronomical Data Analysis Software and Systems V Vol. 101 of Astronomical Society of the Pacific Conference Series, XSPEC: The First Ten Years. p. 17
Aubourg É., Tojeiro R., Jimenez R., Heavens A., Strauss M. A., Spergel D. N., 2008, A&A, 492, 631
Badenes C., Borkowski K. J., Bravo E., 2005, ApJ, 624, 198
Badenes C., Borkowski K. J., Hughes J. P., Hwang U., Bravo E., 2006, ApJ, 645, 1373
Badenes C., Bravo E., Borkowski K. J., Domínguez I., 2003, ApJ, 593, 358
Badenes C., Maoz D., Draine B. T., 2010, MNRAS, 407, 1301
Baldwin J. A., Phillips M. M., Terlevich R., 1981, PASP, 93, 5
Balucinska-Church M., McCammon D., 1992, ApJ, 400, 699
Bell A. R., 1978, MNRAS, 182, 443
Berezhko E. G., Völk H. J., 2004, A&A, 427, 525
Borkowski K. J., Hendrick S. P., Reynolds S. P., 2006, ApJ, 652, 1259
Borkowski K. J., Lyerly W. J., Reynolds S. P., 2001, ApJ, 548, 820
Bozzetto L. M., Filipović M. D., Crawford E. J., Haberl F., Sasaki M., Urošević D., Pietsch W., Payne J. L., de Horta A. Y., Stupar M., Tothill N. F. H., Dickel J., Chu Y.-H., Gruendl R., 2012a, MNRAS, 420, 2588
Bozzetto L. M., Filipovic M. D., Crawford E. J., Payne J. L., de Horta A. Y., Stupar M., 2012b, Rev. Mexicana Astron. Astrofis., 48, 41
Bozzetto L. M., Filipović M. D., Crawford E. J., Sasaki M., Maggi P., Haberl F., Urošević D., Payne J. L., De Horta A. Y., Stupar M., Gruendl R., Dickel J., 2013, MNRAS
Bozzetto L. M., Filipovic M. D., Urosevic D., Crawford E. J., 2012c, Serbian Astronomical Journal, 185, 25
Chen L.-W., Fabian A. C., Gendreau K. C., 1997, MNRAS, 285, 449
Croom S., Saunders W., Heald R., 2004, Anglo-Australian Observatory Epping Newsletter, 106, 12
Dawson J. R., McClure-Griffiths N. M., Wong T., Dickey J. M., Hughes A., Fukui Y., Kawamura A., 2013, ApJ, 763, 56
de Horta A. Y., Filipović M. D., Bozzetto L. M., Maggi P., Haberl F., Crawford E. J., Sasaki M., Urošević D., Pietsch W., Gruendl R., Dickel J., Tothill N. F. H., Chu Y.-H., Payne J. L., Collier J. D., 2012, A&A, 540, A25
De Luca A., Molendi S., 2004, A&A, 419, 837
di Benedetto G. P., 2008, MNRAS, 390, 1762
Dickel J. R., McIntyre V. J., Gruendl R. A., Milne D. K., 2005, AJ, 129, 790
Dickel J. R., McIntyre V. J., Gruendl R. A., Milne D. K., 2010, AJ, 140, 1567
Dickey J. M., Lockman F. J., 1990, ARA&A, 28, 215
Dwarkadas V. V., Chevalier R. A., 1998, ApJ, 497, 807
Fesen R. A., Blair W. P., Kirshner R. P., 1985, ApJ, 292, 29
Filipović M. D., Haberl F., Pietsch W., Morgan D. H., 2000, A&A, 353, 129
Filipović M. D., Haberl F., Winkler P. F., Pietsch W., Payne J. L., Crawford E. J., de Horta A. Y., Stootman F. H., Reaser B. E., 2008, A&A, 485, 63
Filipovic M. D., Haynes R. F., White G. L., Jones P. A., 1998, A&AS, 130, 421
Foley R. J., Challis P. J., Chornock R., Ganeshalingam M., Li W., Marion G. H., Morrell N. I., Pignata G., Stritzinger M. D., Silverman J. M., Wang X., Anderson J. P., Filippenko A. V., Freedman W. L., Hamuy M., Jha S. W., Kirshner R. P., McCully C., Persson S. E., Phillips M. M., Reichart D. E., Soderberg A. M., 2013, ApJ, 767, 57
Frew D. J., Parker Q. A., 2010, PASA, 27, 129
Freyberg M. J., Briel U. G., Dennerl K., Haberl F., Hartner G. D., Pfeffermann E., Kendziorra E., Kirsch M. G. F., Lumb D. H., 2004, in Flanagan K. A., Siegmund O. H. W., eds, Society of Photo-Optical Instrumentation Engineers (SPIE) Conference Series Vol. 5165 of Society of Photo-Optical Instrumentation Engineers (SPIE) Conference Series, EPIC pn-CCD detector aboard XMM-Newton: status of the background calibration. pp 112–122
Gooch R., 1995, in Shaw R. A., Payne H. E., Hayes J. J. E., eds, Astronomical Data Analysis Software and Systems IV Vol. 77 of Astronomical Society of the Pacific Conference Series, Space and the Spaceball. p. 144
Grondin M.-H., Sasaki M., Haberl F., Pietsch W., Crawford E. J., Filipović M. D., Bozzetto L. M., Points S., Smith R. C., 2012, A&A, 539, A15
Haberl F., Filipović M. D., Bozzetto L. M., Crawford E. J., Points S. D., Pietsch W., De Horta A. Y., Tothill N., Payne J. L., Sasaki M., 2012, A&A, 543, A154
Haberl F., Pietsch W., 1999, A&AS, 139, 277
Hambly N. C., Irwin M. J., MacGillivray H. T., 2001, MNRAS, 326, 1295
Hamilton A. J. S., Sarazin C. L., Chevalier R. A., 1983, ApJS, 51, 115
Harris J., Zaritsky D., 2009, AJ, 138, 1243
Hendrick S. P., Borkowski K. J., Reynolds S. P., 2003, ApJ, 593, 370
Hughes A., Staveley-Smith L., Kim S., Wolleben M., Filipović M., 2007, MNRAS, 382, 543
Hughes J. P., Ghavamian P., Rakowski C. E., Slane P. O., 2003, ApJ, 582, L95
Hughes J. P., Hayashi I., Koyama K., 1998, ApJ, 505, 732
Iwamoto K., Brachwitz F., Nomoto K., Kishimoto N., Umeda H., Hix W. R., Thielemann F.-K., 1999, ApJS, 125, 439
Jansen F., Lumb D., Altieri B., Clavel J., Ehle M., Erd C., Gabriel C., Guainazzi M., Gondoin P., Much R., Munoz R., Santos M., Schartel N., Texier D., Vacanti G., 2001, A&A, 365, L1
Jordan IV G. C., Perets H. B., Fisher R. T., van Rossum D. R., 2012, ApJ, 761, L23
Kahn F. D., 1975, in International Cosmic Ray Conference Vol. 11 of International Cosmic Ray Conference, Supernova Remnants. p. 3566
Katayama H., Takahashi I., Ikebe Y., Matsushita K., Freyberg M. J., 2004, A&A, 414, 767
Kavanagh P. J., Sasaki M., Points S. D., Filipović M. D., Maggi P., Bozzetto L. M., Crawford E. J., Haberl F., Pietsch W., 2013, A&A, 549, A99
Kawamura A., Mizuno Y., Minamidani T., Filipović M. D., Staveley-Smith L., Kim S., Mizuno N., Onishi T., Mizuno A., Fukui Y., 2009, ApJS, 184, 1
Kim S., Dopita M. A., Staveley-Smith L., Bessell M. S., 1999, AJ, 118, 2797

Kim S., Staveley-Smith L., Dopita M. A., Freeman K. C., Sault R. J., Kesteven M. J., McConnell D., 1998, ApJ, 503, 674
Kim S., Staveley-Smith L., Dopita M. A., Sault R. J., Freeman K. C., Lee Y., Chu Y.-H., 2003, ApJS, 148, 473
Kosenko D., Helder E. A., Vink J., 2010, A&A, 519, A11
Kromer M., Fink M., Stanishev V., Taubenberger S., Ciaraldi-Schoolman F., Pakmor R., Röpke F. K., Ruiter A. J., Seitenzahl I. R., Sim S. A., Blanc G., Elias-Rosa N., Hillebrandt W., 2013, MNRAS, 429, 2287
Kuntz K. D., Snowden S. L., 2008, A&A, 478, 575
Kuntz K. D., Snowden S. L., 2010, ApJS, 188, 46
Lazendic J. S., Slane P. O., 2006, ApJ, 647, 350
Lee J.-J., Park S., Hughes J. P., Slane P. O., Burrows D. N., 2011a, ApJ, 731, L8
Lee J.-J., Park S., Hughes J. P., Slane P. O., Burrows D. N., 2011b, ApJ, 731, L8
Lewis I. J., Cannon R. D., Taylor K., Glazebrook K., Bailey J. A., Baldry I. K., Barton J. R., Bridges T. J., Dalton G. B., Farrell T. J., Gray P. M., Lankshear A., McCowage C., Parry I. R., Sharples R. M., Shortridge K., Smith G. A., Stevenson J., Straede J. O., Waller L. G., Whittard J. D., Wilcox J. K., Willis K. C., 2002, MNRAS, 333, 279
Lewis K. T., Burrows D. N., Hughes J. P., Slane P. O., Garmire G. P., Nousek J. A., 2003, ApJ, 582, 770
Lumb D. H., Warwick R. S., Page M., De Luca A., 2002, A&A, 389, 93
Maggi P., Haberl F., Bozzetto L. M., Filipović M. D., Points S. D., Chu Y.-H., Sasaki M., Pietsch W., Gruendl R. A., Dickel J., Smith R. C., Sturm R., Crawford E. J., De Horta A. Y., 2012, A&A, 546, A109
Mannucci F., Della Valle M., Panagia N., 2006, MNRAS, 370, 773
Maoz D., 2008, MNRAS, 384, 267
Maoz D., Mannucci F., Li W., Filippenko A. V., Della Valle M., Panagia N., 2011, MNRAS, 412, 1508
Marietta E., Burrows A., Fryxell B., 2000, ApJS, 128, 615
Mathewson D. S., Clarke J. N., 1973, ApJ, 180, 725
Matteucci F., Greggio L., 1986, A&A, 154, 279
Mills B. Y., Turtle A. J., Little A. G., Durdin J. M., 1984, Australian Journal of Physics, 37, 321
Mink D. J., Wyatt W. F., 1995, in Shaw R. A., Payne H. E., Hayes J. J. E., eds, Astronomical Data Analysis Software and Systems IV Vol. 77 of Astronomical Society of the Pacific Conference Series, EMSAO: Radial Velocities from Emission Lines in Spectra. p. 496
Nevalainen J., Markevitch M., Lumb D., 2005, ApJ, 629, 172
Nishiuchi M., Yokogawa J., Koyama K., Hughes J. P., 2001, PASJ, 53, 99
Ohnishi T., Koyama K., Tsuru T. G., Masai K., Yamaguchi H., Ozawa M., 2011, PASJ, 63, 527
Parker Q. A., Bland-Hawthorn J., 1998, PASA, 15, 33
Parker Q. A., Phillipps S., Pierce M. J., Hartley M., Hambly N. C., Read M. A., MacGillivray H. T., Tritton S. B., Cass C. P., Cannon R. D., Cohen M., Drew J. E., Frew D. J., Hopewell E., Mader S., Malin D. F., Masheder M. R. W., Morgan D. H., Morris R. A. H., Russeil D., Russell K. S., Walker R. N. F., 2005, MNRAS, 362, 689
Read A. M., Ponman T. J., 2003, A&A, 409, 395
Reid W. A., Parker Q. A., 2006a, MNRAS, 365, 401
Reid W. A., Parker Q. A., 2006b, MNRAS, 373, 521
Reid W. A., Parker Q. A., 2012, MNRAS, 425, 355
Reid W. A., Parker Q. A., 2013, MNRAS, 436, 604
Rho J., Petre R., 1998, ApJ, 503, L167
Russell S. C., Dopita M. A., 1992a, ApJ, 384, 508
Russell S. C., Dopita M. A., 1992b, ApJ, 384, 508
Sabbadin F., Minello S., Bianchini A., 1977, A&A, 60, 147
Sabin L., Parker Q. A., Contreras M. E., Olguín L., Frew D. J., Stupar M., Vázquez R., Wright N. J., Corradi R. L. M., Morris R. A. H., 2013, MNRAS, 431, 279
Sasaki M., Plucinsky P. P., Gaetz T. J., Smith R. K., Edgar R. J., Slane P. O., 2004, ApJ, 617, 322
Sault R. J., Teuben P. J., Wright M. C. H., 1995, in Shaw R. A., Payne H. E., Hayes J. J. E., eds, Astronomical Data Analysis Software and Systems IV Vol. 77 of Astronomical Society of the Pacific Conference Series, A Retrospective View of MIRIAD. p. 433
Sault R. J., Wieringa M. H., 1994, A&AS, 108, 585
Saunders W., Bridges T., Gillingham P., Haynes R., Smith G. A., Whittard J. D., Churilov V., Lankshear A., Croom S., Jones D., Boshuizen C., 2004, in Moorwood A. F. M., Iye M., eds, Society of Photo-Optical Instrumentation Engineers (SPIE) Conference Series Vol. 5492 of Society of Photo-Optical Instrumentation Engineers (SPIE) Conference Series, AAOmega: a scientific and optical overview. pp 389–400
Seward F. D., Williams R. M., Chu Y.-H., Dickel J. R., Smith R. C., Points S. D., 2006, ApJ, 640, 327
Sharp R., Saunders W., Smith G., Churilov V., Correll D., Dawson J., Farrel T., Frost G., Haynes R., Heald R., Lankshear A., Mayfield D., Waller L., Whittard D., 2006, in Society of Photo-Optical Instrumentation Engineers (SPIE) Conference Series Vol. 6269 of Society of Photo-Optical Instrumentation Engineers (SPIE) Conference Series, Performance of AAOmega: the AAT multipurpose fiber-fed spectrograph
Shull J. M., van Steenberg M., 1982, ApJS, 48, 95
Smith C., Points S., Winkler P. F., 2006, NOAO Newsletter, 85, 6
Snowden S. L., Mushotzky R. F., Kuntz K. D., Davis D. S., 2008, A&A, 478, 615
Strüder L., Briel U., Dennerl K., Hartmann R., Kendziorra E., Meidinger N., Pfeffermann E., Reppin C., Aschenbach B., Bornemann W., Bräuninger H., Burkert W., Elender M., Freyberg M., Haberl F., et al. 2001, A&A, 365, L18
Stupar M., Parker Q. A., 2012, MNRAS, 419, 1413
Sullivan M., Le Borgne D., Pritchet C. J., Hodsman A., Neill J. D., Howell D. A., Carlberg R. G., et al. 2006, ApJ, 648, 868
Turner M. J. L., Abbey A., Arnaud M., Balasini M., Barbera M., Belsole E., Bennie P. J., Bernard J. P., Bignami G. F., Boer M., Briel U., Butler I., et al. 2001, A&A, 365, L27
van der Heyden K. J., Bleeker J. A. M., Kaastra J. S., 2004, A&A, 421, 1031
van der Heyden K. J., Bleeker J. A. M., Kaastra J. S., Vink J., 2003, A&A, 406, 141
van der Marel R. P., Cioni M.-R. L., 2001, AJ, 122, 1807
Vink J., 2012, A&A Rev., 20, 49
Williams R. M., Chu Y.-H., 2005, ApJ, 635, 1077
Williams R. M., Chu Y.-H., Dickel J. R., Gruendl R. A., Shelton R., Points S. D., Smith R. C., 2004, ApJ, 613, 948
Wilms J., Allen A., McCray R., 2000, ApJ, 542, 914

Wong T., Hughes A., Ott J., Muller E., Pineda J. L., Bernard J.-P., Chu Y.-H., Fukui Y., Gruendl R. A., Henkel C., Kawamura A., Klein U., Looney L. W., Maddison S., Mizuno Y., Paradis D., Seale J., Welty D. E., 2011, ApJS, 197, 16
Yamaguchi H., Ozawa M., Koyama K., Masai K., Hiraga J. S., Ozaki M., Yonetoku D., 2009, ApJ, 705, L6
Yamauchi S., Nobukawa M., Koyama K., Yonemori M., 2013, PASJ, 65, 6
Zaritsky D., Harris J., Thompson I. B., Grebel E. K., 2004, AJ, 128, 1606
Zhang Y.-Y., Reiprich T. H., Finoguenov A., Hudson D. S., Sarazin C. L., 2009, ApJ, 699, 1178

APPENDIX A: X-RAY BACKGROUND

In the case of single and double-pixel events, the X-ray background comprises particle-induced and astrophysical components, as well as electronic read-out noise. The particle-induced background of the EPIC consists of three components. The first of these is the quiescent particle background (QPB), a continuum component produced by the direct interaction of penetrating high-energy particles with the detector. Depending on the energy range considered, this can be modelled by a power law not folded through the instrumental response (see Freyberg et al. 2004, Nevalainen et al. 2005, Zhang et al. 2009; for example). The second component consists of the instrumental fluorescence lines, which are due to the interaction of high-energy particles with the material surrounding the detector (Lumb et al. 2002, Read & Ponman 2003). Below 5 keV, only the Al Kα instrumental fluorescence line at 1.49 keV contributes to the EPIC-pn particle-induced background. Finally, we have residual soft proton (SP) contamination, which is due to SPs travelling through the telescope system to the detector. This component is quite variable with periods of high SP background filtered out of an observation event list during a standard reduction. However, there will always remain some residual SP contamination which escapes the filtering criteria and must be considered. The spectrum of these residual SPs can be described by a power-law not convolved with the instrumental response (Kuntz & Snowden 2008), and can vary in both magnitude and slope. The electronic read-out noise is very significant at the lowest energies, increasing dramatically below ~ 0.7 keV. Since we limit our spectral analysis to the 0.4−5 keV energy range, we avoid the most affected energy range; however, some increase in the background is expected just above 0.4 keV.

A1 Quiescent particle background, instrumental fluorescence lines, and electronic read-out noise

To model the QPB, instrumental fluorescence lines, and the electronic read-out noise we make use of the *XMM-Newton* filter wheel closed (FWC) data, which were collected with the detector shielded from the astrophysical and SP backgrounds. A full discussion on the FWC data of the EPIC-pn is given in Freyberg et al. (2004). The FWC data were screened using the same event filtering criteria as for the observational data, and were also vignetting-corrected using the SAS task *evigweight*. Although the QPB is not subject to vignetting, it is necessary to apply the same correction as to the observational data. For the purposes of spectral fitting, ancillary response files are generated for a flat detector map as the effective area correction has already been applied to the event list.

To characterise the FWC spectra, and to assess the likely contribution of the QPB to our observational data, we extract spectra from the FWC data from the same regions of the detector as our SNR source and background spectra. However, these spectra must be scaled to account for differences in the integrated QPB count rates of the observational and FWC data. To perform this scaling we considered the 10–13 keV count rates for the entire field-of-view (FOV) of both datasets and determined a scaling factor. Unless a very bright and hard source is present in the observational FOV, the QPB continuum should dominate both datasets at these high energies. Scaling the FWC data using lower energy range count rates is not safe as there is potentially an astrophysical contribution in the observational data. We selected the energy range 10–13 keV for the scaling as Katayama et al. (2004) showed a good correlation between the 2–7 keV count rate and the 10–13 keV count rate in the FWC observations. Thus, the 10–13 keV count rates can be used to reliably scale the lower energy QPB continuum. The scaled FWC spectra are shown in Figure A1. As previously mentioned, the background spectra were extracted from regions further off-axis than those of the SNR. The fact that these were obtained from a vignetting-corrected FWC dataset has important effects on the normalisations of the QPB components. The vignetting-correction process operates on every event in the data, regardless of photon or particle origin, according to its position on the detector to account for the variation in effective area of the instrument. However, this correction is photon specific and the particle background is not subject to the same effects. This is clearly evident from Fig. A1, with the background spectra having a larger normalisation than their corresponding source spectra due to the higher vignetting-correction applied to events further off-axis.

We chose not to subtract these FWC spectra from the observational spectra because, as pointed out by Kuntz & Snowden (2008) and Snowden et al. (2008), the fluorescence lines of the EPIC instruments are sufficiently strong that small gain variations and differences in environment between FWC and filter wheel open positions can produce significant differences in the lines and correspondingly large residuals after subtraction. Hence, we chose instead to explicitly model the background in our spectral fits, using the FWC spectra shown in Fig. A1 as a basis. We fit models to the FWC spectra simultaneously, allowing only normalisations to vary, and found that the QPB continuum and electronic read-out noise components in the 0.4–4 keV range were best-fit using a broken power law (*bknpower* in XSPEC) not folded through the instrument response, with the energy break (E_{break}) = 0.62 keV, the photon index for $E < E_{break}$ (Γ_1) = 1.91, the photon index for $E > E_{break}$ (Γ_2) = 0.45, and reduced χ^2 = 1.02 for 1363 d.o.f.. Here, Γ_1 represents the electronic read-out noise and Γ_2 the QPB. While at lower energies the electronic read-out noise component requires a more complicated model, in the 0.4-5 keV en-

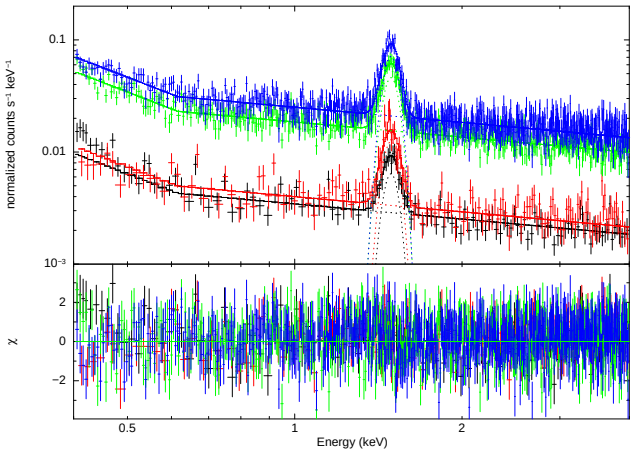

Figure A1. Filter wheel closed spectra extracted from the same source and background regions defined for the X-ray spectral analysis of MCSNR J0508–6902. The black, red, green, and blue data points correspond to the SNR centre, centre background, SNR shell, and shell background, respectively. The best-fit broken power law plus Gaussian line (*bknpower+gauss* in XSPEC) model is indicated by the solid lines ($\Gamma_1 = 1.91$, $\Gamma_2 = 0.45$, and $E_{break} = 0.62$ keV). The difference in normalisations between the corresponding source and background spectra is due to the vignetting-correction process (see text).

ergy range we consider, a power-law is sufficient. A Gaussian line was also included to account for the Al Kα instrumental fluorescence line at 1.49 keV. The fits to the FWC spectra are indicated in Fig. A1 as the solid lines. Above 4-5 keV, the defined model no longer applies as the QPB 'flattens'. However, this is unimportant in our analysis as we can easily constrain the QPB model given that this component dominates the emission above 1.5-2 keV. In our spectral analysis of MCSNR J0508–6902, the ratios of the normalisations of the source and background QPB components were fixed to the values determined from the QPB spectra.

A2 Soft-proton contamination

To account for the residual SP contamination in our spectra, we included the appropriate power law model not convolved with the instrument response. However, the fits would consistently return a zero normalisation for the SP component, suggesting that the SP contamination is not significant. This could be expected given the fact that there were no SP flares during the observation. However, we note that a lack of SP flares does not necessarily mean no significant SP contamination. Thus, we ran the diagnostic algorithm of De Luca & Molendi (2004)[8] which suggested little or no contamination by SPs. A further indication that SP contamination is minimal is that the shell spectrum above 2 keV, where we expect the SP contamination to be most noticeable, can be accounted for by the QPB component, with the normalisation of the QPB components in all our fits agreeing with those of the FWC spectra within their 90% confidence intervals. For these reasons, we conclude that residual SPs have no significant effect on our spectra and we ignore their contribution in our analysis.

A3 Astrophysical background

The astrophysical background can usually be modelled with four or fewer components (Snowden et al. 2008, Kuntz & Snowden 2010). These are: the unabsorbed thermal emission from the Local Hot Bubble (LHB, $kT \sim 0.1$ keV), absorbed cool ($kT \sim 0.1$ keV) and warm ($kT \sim 0.25$ keV) thermal emission from the Galactic halo, and an absorbed power law representing unresolved background cosmological sources ($\Gamma \sim 1.46$, Chen et al. 1997). The cool Galactic halo component likely does not contribute to the astrophysical background in this case as it is absorbed by the foreground Galactic absorbing column and, thus, we do not consider it in our background models. During our analysis, we allowed the LHB and warm Galactic halo temperatures to vary, with the spectral index of the unresolved background power-law fixed at 1.46. Additionally, it was assumed that the temperature of the thermal components and the surface brightness of the thermal and non-thermal components did not vary significantly between the source and background regions. Thus, the appropriate temperature and normalisation parameters were linked. To model the absorption of the Galactic halo and cosmological background sources we used a photoelectric absorption model in XSPEC. The Galactic halo emission is subject to foreground Galactic absorption ($N_{\rm H\ Gal}$), which was fixed at 7×10^{20} cm^{-2} based on the HI maps of Dickey & Lockman (1990). The unresolved cosmological background component is not only subject to this Galactic absorption, but also absorption by material in the LMC ($N_{\rm H\ LMC}$). This LMC absorption component was incorporated into the fits using a *vphabs* model with abundance at 0.5 solar as appropriate for the LMC (Russell & Dopita 1992b). However, the formal best-fit value of $N_{\rm H\ LMC}$ invariably tended to zero and was ultimately fixed as so. The astrophysical background was sufficiently accounted for by our defined model, the best-fit parameters of which were consistent in all of our fits. The temperature of the LHB and warm Galactic halo components were (0.08–0.11) keV and (0.28–0.33) keV, respectively, which are compatible the expected values from Snowden et al. (2008) and Kuntz & Snowden (2010).

[8] See `http://xmm2.esac.esa.int/external/xmm_sw_cal/background/epic_scripts.shtml`